ABSTRACT

Title of dissertation:	PREDICTIONS REGARDING THE PERFORMANCE OF FIELD EMISSION CATHODES IN RADIO FREQUENCY GUNS
	Mathew Virgo, Doctor of Philosophy, 2010
Dissertation directed by:	Professor Patrick O'Shea Department of Electrical and Computer Engineering

Recent technological advances have generated interest in using a field emission cathode in a radio-frequency (RF) electron gun. One of the necessary steps towards the realization of this concept is to establish a comprehensive understanding of the electron distribution produced by such a cathode, and the goal of this work is to expand this body of knowledge. For the specific case of ungated field emitter arrays, we investigate aspects of the temporal and transverse electron distribution, as well as the relationship between emission timing and the ensuing acceleration of the electrons.

We show that an upper bound can be placed on the magnitude of the transverse momentum imparted to the electrons by the nonlinear accelerating forces that exist close to the emitter tips. This establishes a limit on the cathode's intrinsic emittance, an important determining factor for beam quality. We examine the consequences of this result in the context of relevant theoretical and experimental

studies reported in the literature. This is followed by a series of calculations based on a simple emitter model, which are used to study specific aspects of the transverse momentum distribution. Our focus then shifts to the longitudinal beam dynamics. An examination of the on-axis trajectories demonstrates that it is possible to design a gun such that essentially all of the field-emitted current reaches the exit of the cavity. This indicates a source of this type may be capable of producing high average beam power. In the final chapter, the properties of ungated field emission cathodes are compared with the properties of cathodes that are typically used in RF guns. This gives some insight into how the field emission cathode might perform in this setting.

PREDICTIONS REGARDING THE PERFORMANCE OF FIELD EMISSION CATHODES IN RADIO FREQUENCY GUNS

by

Mathew Virgo

Dissertation submitted to the Faculty of the Graduate School of the
University of Maryland, College Park in partial fulfillment
of the requirements for the degree of
Doctor of Philosophy
2010

Advisory Committee:
Professor Patrick O'Shea, Advisor
Dr. Sandra Biedron, Argonne National Laboratory
Professor Daniel Lathrop
Professor Wes Lawson
Professor John Melngailis

Dedication

To Dorna and Richard Virgo

Acknowledgments

To begin with, I wish to thank my fellow students in the group, Yupeng Cui, Hui Li, John Harris, and Jon Neumann. Working with them was both rewarding and enjoyable. I'm also grateful to Nate Moody and Eric Montgomery, *i migliori fabbri*, who built so successfully on the shaky foundation I left for them. Jay Pyle's giftedness at teaching shop skills was nearly a match for my deficiencies as a student. Brian Quinn provided substantial assistance in the lab, and John Rogers, whose expertise seem limitless, gave me invaluable advice on electronics and diagnostics. Rami Kishek was an adroit teacher with an extensive knowledge of beam physics, a fact I wish I had taken more advantage of. Santiago Bernal's boundless enthusiasm for physics was augmented with a dry and unpredictable sense of humor; between the two there was never a dull moment.

At IREAP, I thank Carol Bellamy, Nancy Boone, Margaret Hess, and Janice Schoonover for their assistance. Dottie Brosius developed the excellent template I used to write this document. I am indebted to Tracy Chung, Maria Hoo, and Melanie Prange in the graduate studies office, who rescued me, more frequently than they should have had to, when I missed a deadline or overlooked a requirement. At Argonne, I would be completely lost if I didn't have Raquel Young, Lydia Koehl, and Denise Voss to help me navigate the system.

I wish to thank the Office of Naval Research and Quentin Saulter for giving me the opportunity to work on several highly rewarding projects. Furthermore, I wish to thank the High Energy Laser Joint Technology Office, and its Navy representative,

Several colleagues and mentors have gone out of their way to help me succeed over the years. These include Peter Tofilon, Jeff Sullivan, and Victor Yun. Victor helped me immensely in the lab, and he also encouraged me to get out of the lab with regular biking expeditions. I count myself extremely lucky to be one of the innumerable beneficiaries of John Noonan's mentoring. Don Feldman's curiosity is apparently inexhaustible, and his experience is vast; it was a privilege to work with him and learn from him, and it was also a great deal of fun. I must also note a great debt of gratitude to Renée Feldman, who was exceptionally generous to me (as she was to everyone). Her thoughtful words of encouragement helped me keep things in perspective whenever I felt like I was in over my head.

I have never met anyone so determined and energetic as Sandra Biedron, and I don't think I ever will. Sandra approaches obstacles with the same subtlety a chipper-shredder approaches a tree branch. As my supervisor at Argonne, she not only accommodated and encouraged me to finish my dissertation, she practically insisted. Without her tireless exhortation, I never would have made it to this point.

Finally, I wish to thank Patrick O'Shea. It has been my great fortune to have him as an advisor. To me, the most significant lessons I've learned from him have been the most universal. I've learned to consider a question or problem carefully before attempting a solution. Also through Pat's influence, I've come to have greater respect for other people's viewpoints. Because of him, my experience in graduate school has truly been a formative one.

Table of Contents

List of Figures

List of Abbreviations

CVD	chemical vapor deposition
DFEA	diamond field emitter array
FEA	field emitter array
FEL	free electron laser
FWHM	full width at half maximum
ODE	ordinary differential equation
RF	radio frequency
RMS	root mean squared
SEM	scanning electron microscope
TE	transverse electric
TM	transverse magnetic

Chapter 1

Introduction

1.1 Motivation

This dissertation describes the exploration of a field emission electron source in a radio-frequency (RF) electron gun. High energy, short pulse electron beams have important technological applications, such as particle colliders and beam-based light sources. The electron source is a critical component of the accelerators used to produce these beams. The RF gun, which consists of a cathode mounted in an RF cavity, is a commonly used type of electron source. This configuration has the advantage that a very strong accelerating field, typically from several MV/m to 100 MV/m, can be generated at the surface of the cathode. As a result, the electrons are rapidly accelerated to relativistic energies, which makes the bunch less susceptible to the deleterious effects of interelectron forces and stray fields.

There are three main mechanisms for electron emission: thermionic emission, field emission, and photoemission. Thermionic cathodes and photocathodes are both frequently used in RF-guns. Though guns based on both of those cathode types have many desirable characteristics, each has inherent limitations. For thermionic cathode RF guns, peak current is limited by thermal emission and average current is limited by potential back-bombardment that can destroy the cathode as the field reverses. Photocathode RF guns can produce very high peak current, but metal

photocathodes require high laser powers to overcome the low quantum efficiencies and non metal photocathodes have low lifetimes often caused by contamination in the high field environments with less than optimal/compatible vacuum.

Until now, technological limitations have precluded the use of field emission cathodes in RF guns, but new fabrication techniques have been developed that produce cathodes that appear to be suitable for this application. A field emission cathode gun has the potential to generate higher peak and average currents than the thermionic cathode gun, and its simplicity (for example, a drive laser is not needed) would exceed either existing gun type.

To build a gun based on a field emission cathode, the characteristics of its emission must be well understood. In this dissertation, we study the dynamics of electrons emitted from field emission cathodes – specifically for the case of bare (ungated) emitters in an RF gun – using both analytical calculations and numerical examples. This information will be useful for identifying applications for which this type of gun could be used, for designing appropriate cavities, and for interpreting experimental results.

1.2 Electron sources for RF accelerators

1.2.1 Beam requirements for RF acceleration

RF acceleration is fundamental to the the generation of high quality high energy electron beams. In this approach, an RF cavity is excited with a mode with a longitudinal electric field component along its axis. Electron bunches are

synchronized to arrive when the polarity of the field pushes the electrons in their direction of travel. The electrons exit the cavity before the polarity of the field reverses. In this manner, the electrons experience a strong push over an extended distance. Cavities are added in series to achieve the desired beam energy.

Because the magnitude of the field is continuously changing as the electron passes through an accelerating cavity, the momentum gain imparted to a given electron is a function of the time it enters the cavity. Therefore, the pulse length of the beam must be short compared to the RF period in order to preserve a limited momentum spread. In practical terms, the maximum bunch length is limited to a little more than one degree of phase. This translates to about 5 ps for the popular 2.85 GHz (S-band) frequency. 1.3 GHz (L-band) accelerators correspondingly support pulses roughly twice as long. Electron sources for RF accelerators are required to produce pulses with this temporal profile.

1.2.2   Sources of bunched beams

One common electron source consists of a gun with a DC or pulsed field and a thermionic cathode. Once generated, the beam must be chopped and compressed to the necessary length (RF bunching). The disadvantage of this approach is that much of the charge is discarded, and the beam quality is degraded during the conditioning process. A significant advantage in this regard can be gained by replacing the thermionic cathode with a photocathode. A short pulse laser can than be used to generate a similarly short pulse directly from the cathode.

An alternate type of electron source is the thermionic cathode RF gun [1]. In the usual case, a cylindrical (pillbox) cavity is excited at the TM_{010} mode, which has a longitudinal electric field component on-axis that accelerates the electrons. Current is extracted from the cathode following the sinusoidal oscillation of the field. However, the path each electron takes depends strongly on the phase of the field when it is emitted, and most of the charge does not escape the cavity. The result is a steady stream of pulses, the details of which are determined by properties such as the magnitude of the field and the length of the cavity. Because higher fields are possible in an RF cavity than can be achieved in a DC gun, the peak current is greater, and because the bunch spends less time at low energy, the beam quality is better. A thermionic cathode RF gun is usually followed by a device called an α-magnet, which compresses the pulse, and can also remove part of the beam to reduce the energy spread.

Yet another type of electron source is the RF photocathode gun [2], illustrated in figure 1.1. Instead of a thermionic cathode, a photocathode is installed in the
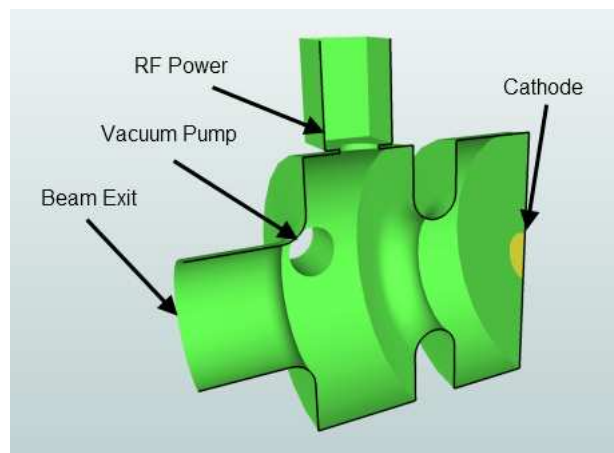
Figure 1.1: Components of an RF gun.

4

RF cavity. By gating the emission with a short-pulse laser, short, very high current pulses with low energy spread are generated. These are highly desirable properties for many beam applications, notably the generation of coherent radiation, where peak current drives the efficiency of the process. The timing of the emission can be controlled relative to the RF phase to optimize the beam dynamics, and the profile of the laser pulse can be adjusted to tailor the beam distribution. The main disadvantage of the photocathode gun is complexity. Sophisticated lasers are required to drive the cathode, and many types of photocathodes require extensive preparation.

1.3   Pillbox cavities

Most RF guns are some variation on a pillbox cavity, which is simply a right circular cylinder capped at both ends. The modes supported by the cavity are determined by solving the Helmoltz equation for this geometry with conducting boundary conditions. Two distinct types of solutions are possible: transverse electric (TE) modes and transverse magnetic (TM) modes. TM modes have an axial electric field component; it is this component of the field that accelerates the electrons in an RF gun. The order of the mode is specified by the set of three numbers m, n, and p. m specifies the azimuthal component, m and n together specify the radial component, and p specifies the longitudinal component. The TM_{010} mode is the lowest order TM mode. This mode has a longitudinal electric field component E_z that does not depend on z. This is the specific mode that is used in RF guns. The

fields are [3]

$$E_z = E_0 \, J_0 \left(2.405 \frac{r}{R} \right) \cos \left(\omega t \right) \tag{1.1}$$

$$H_\phi = -\sqrt{\frac{\epsilon_0}{\mu_0}} E_0 \, J_1 \left(2.405 \frac{r}{R} \right) \sin \left(\omega t \right) \tag{1.2}$$

where R is the radius of the cavity and 2.405 is an approximation for the first root of the Bessel function of order zero. The resonant frequency of this mode is $\omega_{010} = 2.405 c / R$ where c is the speed of light. We see that the resonant frequency for this mode is independent of the cavity length.

1.4   Beam transport and beam quality

1.4.1   Beam transport concepts

In a rough sense, beam quality is usually thought of in terms of how readily the beam can be confined in the spatial dimensions during its flight and the closely related question of how small a spot the beam can be focused to. These properties determine, for instance, how many collisions occur when two beams intersect in a collider, and how efficiently the electron beam interacts with the optical mode in a free electron laser. In this section, we will look at how beam quality can be defined quantitatively. We will explain why it is generally difficult or impossible to improve certain measures of beam quality during transport. This issue underlies the importance of understanding the mechanics of emission of electrons from the cathode.

For the transport of relativistic beams, magnetic lenses are used. The most

common elements are dipoles for steering and solenoids and quadrupoles for focusing. To first order, these are linear elements; they give the electron a transverse kick in linear proportion to its transverse position. In many cases, these lenses can be approximated as thin lenses, where the details of the dynamics are ignored, and the electron is viewed as receiving an instantaneous push as it crosses the center of the lens. When, in addition to this, space charge forces are neglected, the electrons travel in straight lines between lenses, and they behave the same as the rays used in geometric optics. In this case, the techniques familiar from geometric optics, such as the use of transfer matrices, can be employed without modification.

Though useful, the limitations on the analogy between optics and beam transport are quickly reached in practical applications. Many elements which exist only in one context or the other, and even "equivalent" elements are often only identical in a low-order approximation. In addition to these specific differences in their technological building blocks, there are also substantial differences way they are assembled into systems. Generally, the problem in optics is to create an image of an object to a certain degree of accuracy. In beam transport, instead of preserving the details of the distribution, the usual goal is to preserve the quality of the distribution in a statistical sense. We next discuss how beam quality is quantified.

1.4.2 Emittance

A particle is identified by its coordinates in the six-dimensional space corresponding to its six mechanical degrees of freedom. An ensemble of particles in this

space constitutes a beam. By definition, the motion of the beam is predominantly in one direction. It is therefore convenient to consider the transverse coordinates as a set and to treat the longitudinal coordinate separately. In this context, the beam can also be defined in four-dimensional trace space where, if x and y are the transverse coordinates and z is the longitudinal one, the coordinates of a particle in trace space are x, dx/dz, y, and dy/dz.

Emittance [4] is a statistical measure of how well-behaved a beam is. Here, we will discuss how it is calculated and why it is significant. Several definitions for emittance are used, but the one we will use is the rms emittance. For each dimension, this quantity is defined as

$$\tilde{\epsilon}_x = \sqrt{\overline{x^2}\,\overline{x'^2} - \overline{xx'}^2} \tag{1.3}$$

where $x' = dx/dz$. In statistical terms, $\overline{xx'}$ is the covariance of x and x'. Pearson's correlation coefficient, which normalizes the covariance to fall between -1 and 1, is a measure of the linear dependence between two variables. Is is given by $r_{a,b} = \overline{ab}/\left(\sqrt{\overline{a^2}}\sqrt{\overline{b^2}}\right)$. Expressed in terms of correlation, the rms emittance becomes

$$\tilde{\epsilon}_x = \sqrt{\overline{x^2}}\sqrt{\overline{x'^2}}\sqrt{1 - r_{x,v_x}^2} \tag{1.4}$$

As an example, during free drift the beam expands, but the effect of the increase in beam size on the rms emittance is offset by the increased correlation between position and velocity. This situation is illustrated figure 1.2.

The rms emittance as defined above changes when the beam is accelerated or
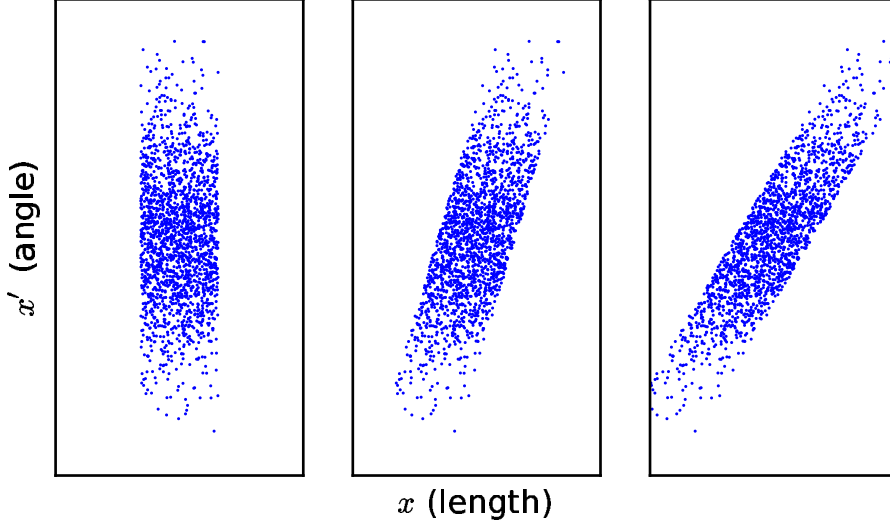
Figure 1.2: x-x' trace space distribution for a beam expanding during drift at three points in time. Initially, the distribution is upright; there is no correlation between position and velocity – the beam is at a waist. As time increases, the distribution tilts, resulting in a widening of the beam in x and increased correlation between x and x'.

decelerated. This can be shown by using the substitution

$$x' = \frac{v_x}{v_z} = \frac{\gamma m v_x}{\gamma m v_z} = \frac{p_x}{p_z}$$

in equation 1.3, where γ is the Lorentz factor and m is the mass of the electron, yielding

$$\tilde{\epsilon}_x = \sqrt{\overline{x^2 \left(\frac{p_x}{p_z}\right)^2} - \overline{x \left(\frac{p_x}{p_z}\right)}^2}.$$

For a beam, p_z is nearly the same for all particles. Furthermore $p_z \gg p_x$, so $p_z \simeq p = \text{const}$. With this approximation,

$$\tilde{\epsilon}_x = \frac{1}{p}\sqrt{\overline{x^2 \, p_x^2} - \overline{x p_x}^2}.$$

The effects of acceleration and deceleration only influence this expression through changes in p. With the relationship $p = mc\beta\gamma$ where c is the speed of light and

9

$\beta = v/c$, the rms emittance becomes

$$\tilde{\epsilon}_x = \frac{1}{\mathrm{mc}\beta\gamma}\sqrt{\overline{x^2}\,\overline{p_x^2} - \overline{xp_x}^2}.$$

From this expression, the *normalized rms emittance,*

$$\tilde{\epsilon}_{n,x} = \beta\gamma\epsilon_x = \frac{1}{\mathrm{mc}}\sqrt{\overline{x^2}\,\overline{p_x^2} - \overline{xp_x}^2}$$

is defined, which contains the same information about the transverse dynamics as the unnormalized value but does not depend on the beam energy. Normalized rms emittance can be used to characterize the intrinsic emittance of a source. Normalized emittance is also referred to as *invariant* emittance.

Emittance determines the smallest size to which a beam can be focused [4], analogously to the way wavelength determines the minimum possible beam waist in Gaussian optics. For a linear system, emittance is conserved [5]. Nonlinear forces, including space charge interactions and nonlinear external fields, can lead to emittance growth, which may be reversible or irreversible. In the context of the RF accelerator, typical normalized rms emittance values are in the range of microns.

1.4.3   Intrinsic emittance of a source

At the source, the velocity distribution is generally independent of position. This will be true for all the cases we consider. In this case, the correlation term is zero. Also, the motion is nonrelativistic, so $p_x = mv_x$. The intrinsic, normalized rms emittance of the source is therefore

$$\tilde{\epsilon}_{s,x} = \frac{1}{\mathrm{c}}\sqrt{\overline{x^2}}\sqrt{\overline{v_x^2}} = \frac{1}{\mathrm{c}}\tilde{x}\,\tilde{v}_x \tag{1.5}$$

where the tildes denote rms values. As an example (see p. 11 of [4]), for a round, thermionic cathode, $\tilde{x} = a/2$ where a is the radius, and, assuming Maxwell-Boltzmann statistics, $\tilde{v}_x = \sqrt{kT/m}$, so

$$\tilde{\epsilon}_{s,x} = \frac{a}{2}\sqrt{\frac{kT}{mc^2}} \qquad \text{(thermionic cathode)} \qquad (1.6)$$

For typical thermionic cathode temperatures, kT is on the order of 100 meV. For a cathode with a radius of 5 mm, this corresponds to $\tilde{\epsilon}_{s,x} = 1.1\ \mu$m.

1.4.4   Brightness

By passing a beam through an aperture, its emittance can be improved at the expense of current. For applications where being able to achieve high current density is necessary, emittance alone does not determine the utility of a beam. For these cases, beam brightness is a valuable figure of merit. The exact expression for brightness depends on the details of the beam distribution and whether the peak or average value is being considered [6, 7]. The general form is

$$B = \frac{1}{\kappa^2 \pi^2} \frac{2I}{\tilde{\epsilon}_x \tilde{\epsilon}_y}$$

where κ is on the order of 3-5. By replacing the emittance with normalized emittance, a normalized brightness is defined:

$$B_n = \frac{1}{\kappa^2 \pi^2} \frac{2I}{\tilde{\epsilon}_{n,y} \tilde{\epsilon}_{n,y}}.$$

As an example of the importance of brightness, for an FEL, it determines the efficiency of the interaction between the electron beam and the optical mode. Though thermionic guns are capable of producing low emittance beams, photocathode guns

11
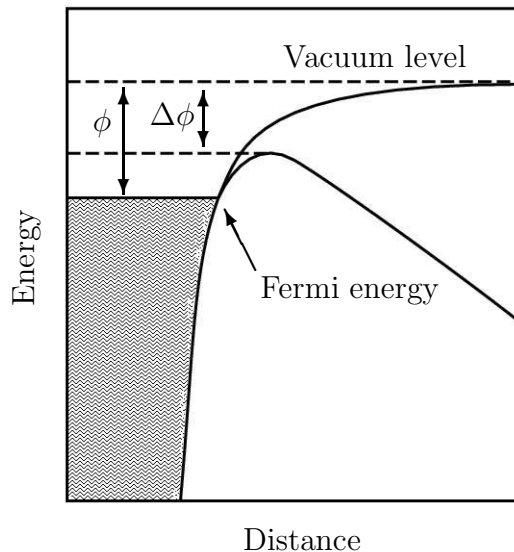
Figure 1.3: Field emission is the emission of electrons that tunnel through the surface barrier with the application of a strong electric field. This figure illustrates the Schottky lowering $\Delta\phi$ of the barrier by the field, where ϕ is the work function of the metal.

have a significant advantage in producing bright beams because a very large number

of electrons can be generated in an extremely short pulse.

1.5 Field emission and FEA cathodes

1.5.1 Fowler-Nordheim equation

Field emission describes the escape of electrons into the vacuum by tunneling

through the surface barrier 1.3. The central equation describing field emission is the

Fowler-Nordheim equation. A basic version of the Fowler-Nordheim equation that

applies to flat, metallic surfaces at zero temperature, is (see, for example, [8]):

$$
\mathrm{J}\left(F\right) = \frac{e^3}{16\pi^2\hbar} \frac{1}{t(y)^2} \frac{F^2}{\phi} \exp\left(-\frac{4}{3}\frac{\sqrt{2\mathrm{m}}}{e\hbar} \, v(y) \, \frac{\phi^{\frac{3}{2}}}{F}\right),
$$

where F is the applied field, e is the electron charge, and ϕ is the work function of the metal. The functions $t(y)$ and $v(y)$ incorporate the effects of Schottky barrier lowering on the electron escape probability [9], where the parameter y is the magnitude of the barrier lowering as a fraction of the work function:

$$y = \frac{1}{\phi}\sqrt{\frac{e^3 F}{4\pi\epsilon_0}}.$$

t and v must be computed numerically. Various approximations have been developed for situations where an analytic expression is needed, and we will use the crudest of these [10]:

$$t(y)^2 = 1.1, \qquad v(y) = 0.95 - y_N^2.$$

With these substitutions, the approximate field emission current density is

$$\mathrm{J}\,(F) \approx \frac{e^3}{16\pi^2\hbar}\frac{1}{1.1}\frac{F^2}{\phi}\exp\left(\frac{4}{3}\frac{1}{4\pi\epsilon_0}\frac{e\sqrt{2m}}{\hbar}\frac{1}{\sqrt{\phi}}\right)\exp\left(-0.95\frac{4}{3}\frac{\sqrt{2m}}{e\hbar}\frac{\phi^{\frac{3}{2}}}{F}\right)$$

The utility of the approximation is seen to be that it simplifies the term in the exponential by separating it into two components, only one of which has a field dependence. The reader is referred to chapter 2, section C2 of the book by Jensen [11] for a discussion of this and other relevant approximations. Because the field is a rapidly changing function of position near a field emitter tip, having a simplified expression for the field emission equation makes calculations involving the current density distribution more manageable (for more context, see section 3.2.2.4 of [12]).

In numerical terms, the equation is

$$\mathrm{J}\,(F) \approx \left(1.4 \times 10^{-6}\,\frac{\mathrm{eV}\,\mathrm{V}^2}{\mathrm{m}^2}\right)\frac{F^2}{\phi}\exp\left(\frac{9.8\,\mathrm{eV}^{\frac{1}{2}}}{\sqrt{\phi}}\right)\exp\left(-6.5 \times 10^9\,\frac{\mathrm{m}}{\mathrm{eV}^{\frac{3}{2}}\mathrm{V}}\frac{\phi^{\frac{3}{2}}}{F}\right)$$

$$(1.7)$$

13

if the field is measured in volts per meter and the work function is measured in electron volts. This equation is plotted in figure 1.4. We note that in this approximation the basic shape of the curve is fixed, with the work function serving to scale the curve in the horizontal and vertical directions.
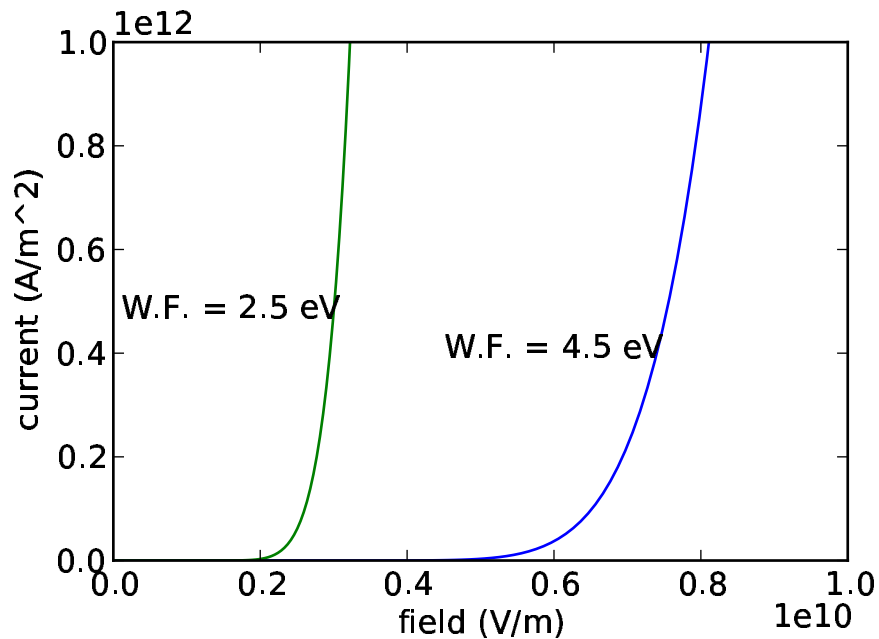
Figure 1.4: Behavior of field emission (Fowler-Nordheim equation) from a flat, metal surface in the low-temperature limit for two values of work function. 4.5 eV is roughly the work function of molybdenum. 10^{12}A/m^2 is considered a very high current density for pulsed operation; 10^{11}A/m^2 is high for DC operation (the limitation is often the melting point of the material). See, for example, chapter two of [13].

As we alluded to above, this form of the Fowler-Nordheim equation is based on several assumptions. When these assumptions are not met, the results break down with various degrees of severity. For instance, this version assumes the metal is at zero temperature. However, the correction at room temperature is minimal. Another issue is that the image charge approximation used to calculate the barrier

lowering breaks down for extremely sharp points [14], though this effect is masked by the fact that the effective emission area is strongly field dependent in this regime. A further qualification is that the derivation assumes a metallic density of states, but it is usually the case that the equation in the above form adequately describes emission from other types of materials [15, 16]. A thorough discussion of all of the conditions and assumptions that lead to the various forms of the Fowler-Nordheim equation and its generalizations can be found in the book by Jensen [11].

1.5.2 Field emitter arrays

For many materials, especially metals, significant field emission requires fields in the range of several gigavolts per meter. Field emission usually only occurs, intentionally or unintentionally, where field enhancement due to sharp features occurs in the presence of a strong applied field. Early experiments in this field used metal wires sharpened into needles by polishing or chemical etching.

Field emitter arrays (FEA) are arrays of tips formed by using deposition and lithography. They were first developed in the middle of the last century following the advent of vacuum deposition techniques. The first FEA was demonstrated by Spindt based on work by Buck and Shoulders (for a historical overview, see, for example, [17, 18]). Spindt cathodes, with tips made of molybdenum, are generally conical in shape, as can be seen in figure 1.5. The processes used to fabricate these cathodes, and others that followed, can produce much sharper tips than earlier field emission sources. As a consequence, lower extraction fields are required. Most FEAs

Cross-section of a tip

v99-146/f6b

— 1 μm —
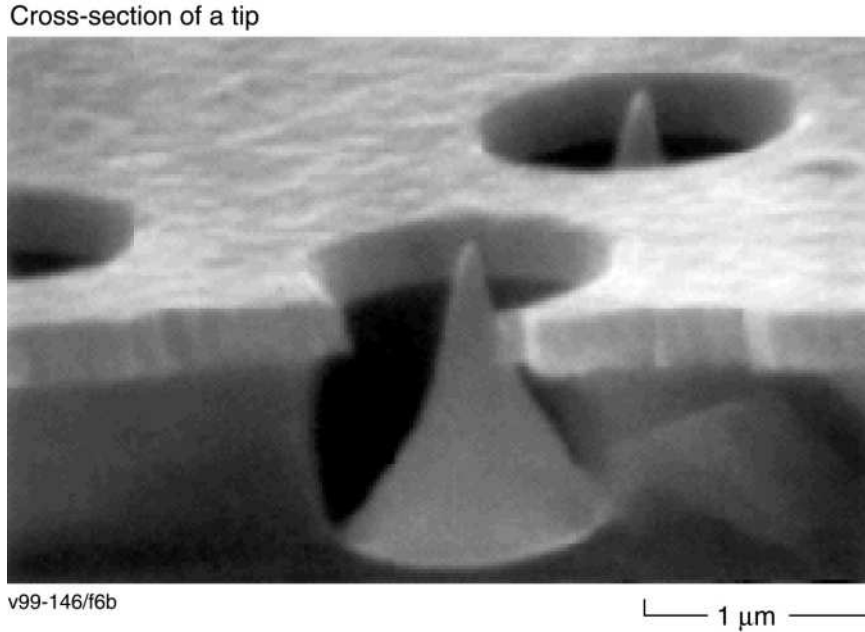
Figure 1.5: Scanning electron microscope (SEM) micrograph of a Spindt cathode. (Courtesy of Capp Spindt, SRI International.)

have integrated gates that are spaced very closely to the tips. This allows high fields to be generated at reasonable voltages, typically on the order of 100 V, though for some types the number is lower.

Since their invention, FEA cathodes have been made from numerous materials using a wide variety of processes. Much of the research had been centered around their potential commercial application as a flat panel display technology [8]. Silicon FEAs are one notably well investigated category of device [16]. Silicon tips can be made sharper than metal ones, and emission occurs at lower fields. Aspects of silicon FEAs that require further development are reliability and the capability to produce devices of larger size. A wide variety of issues related to the fabrication and application of FEAs are reviewed in [19].

The focus of this dissertation is the use of ungated cathodes in an RF gun.

16
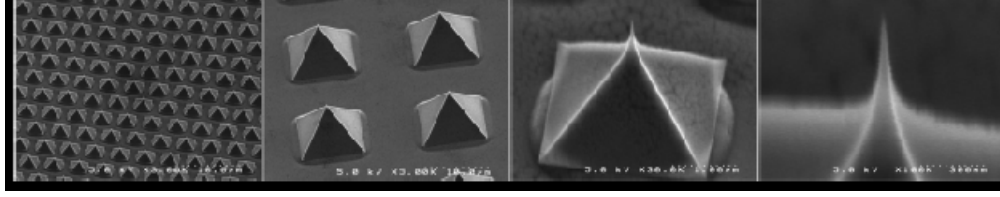
Figure 1.6: SEM micrograph of a diamond pyramid FEA at various degrees of magnification. The nanotip generates significant field enhancement. (Courtesy of Jonathan Jarvis, Vanderbilt University.)

Metal cathodes are not suitable for this application because the fields they require are greater than the peak electric field generated in an RF gun [15]. The main obstacle to the realization of this concept is the lack of a cathode with the requisite combination of ruggedness and low turn-on field. However, recent generations of diamond field emitter arrays (DFEAs) seem to meet those requirements. Diamond is insensitive to surface degradation, and though the emission process is not fully understood, the barrier to emission is lower than most FEA materials [20]. Chemical vapor deposition (CVD) is used to fabricate pyramid shaped structures with sharp, filament-like microtips that provide substantial field enhancement [21]. A CVD diamond DFEA is illustrated in figure 1.6 Current of 15 μA DC per tip and 25 μA pulsed have been demonstrated; values which are reported to be limited by the measurement apparatus [22]. Average current densities above 100 A/cm^2 have been reported [23]. A process for ensuring emission is uniform from tip to tip has been described [24]. The largest array reported was 224×224 [22]. Lastly, the application of these cathodes for a FEL, including their use in an RF gun, has been proposed [23].

17

1.5.3 Operation of FEAs at microwave frequencies

The operational characteristics of FEA cathodes at microwave frequencies has long been a topic of interest [25]. The interest continues today, particularly related to their use in microwave tubes [26]. FEAs offer several benefits, including high current density and fast switching time. For use in space, FEAs have the advantage of not requiring a power-consuming heating element. Low emittance is a particular advantage at the highest frequencies, where the feature sizes of the tubes get very small [27]. Often in RF applications, capacitance between the tips and the gate, which puts a limit on the attainable modulation frequency, is a primary concern. Because we are considering ungated cathodes, this is not an issue for us. A result from this area of research that does have implications for our investigation is the demonstration that the emission process itself is not altered at microwave frequencies [13].

1.5.4 Physical properties

The results we will describe are highly dependent on the geometry of the emitters. FEA tips exist in a very wide variety of shapes and sizes. Spindt emitters are roughly conical [10], whereas many silicon FEAs [28] and some diamond emitters [21] are pyramid-shaped. Carbon nanotubes, whose small tip radii lead to very high field enhancement factors, are another well investigated species of emitter. For descriptions of a wide variety of emitter types, see [19]. Spindt emitters and the pyramid shaped structures have tapered cross sections, often with a sharp protrusion at the

apex known as a microtip or nanotip (see figure 1.5). The small radius of curvature of the microtip gives these emitters their high field enhancement factors. We will, in general, concentrate on structures that are roughly 1 μm tall with moderate aspect ratios, which is representative of many of the most common FEAs. An exception will be made for TaSi$_2$ rods, which are very tall relative to their radius, because their intrinsic emittance has been measured [39]

1.6   Concept of a field emission cathode-based RF gun

The idea of using a field emitter cathode in an RF gun has been suggested, but no successful implementation has been reported. In many cases, even the concepts that have been proposed have appeared in the literature only indirectly [30]. In the 1990's, the design of a reentrant half cell S band cavity intended as a test bed for this application was reported by researchers from Dortmund University and University of Wuppertal [31], but no later mention of this project could be found.

In many ways, the properties of an FEA cathode-based RF gun would be intermediate between the thermionic cathode gun and the photocathode gun. Compared to the thermionic cathode case, there is potential for higher brightness, and the phenomenon of back bombardment would be reduced or, possibly, eliminated. Compared to the photocathode gun, the brightness would be lower, and there would not be the same degree of control over the pulse shape and timing. In simplicity of operation, the FEA based gun would have an advantage over either existing technology.

The possible approaches for incorporating a field emission cathode in an RF gun can be broadly divided into two categories: those based on gated cathodes, and those based on ungated ones. The advantages of gated cathodes for this application are independent control of the timing of the emission, general separation of the field in the gun from the field used to drive the cathode, and the potential to use the gate electrode or electrodes as a lens to collimate each beamlet individually, which would greatly improve overall beam quality. A possible impediment to this approach is that, as discussed above, the capacitance between the tips and the gate limit the switching frequency (Jensen [15] has discussed this issue in this context). Also, the current absorbed by the grid could be of a magnitude where thermal management would become a challenge. In general, the gated case is more complex, though not necessarily prohibitively so.

The work reported in this dissertation is entirely focused on the ungated case, the advantages and disadvantages of which are basically opposite to those of the gated emitter. The setup is simpler, but there is no way to control the emission independently of the accelerating field. Emission is peaked at the crest of the field, which is not optimal for the beam dynamics. Though the emittance of each beamlet is small because the emission area is small and the transverse velocity is correlated with position, there is no mechanism for collimating the beamlets before they merge, at which point the correlation is lost leading to an irreversible increase in the emittance.

In a recent paper, Lewellen and Noonan [32] proposed a novel RF gun design based on a field emission cathode that exhibits many of the desirable characteristics

of both thermionic cathode and photocathode-based RF guns. The idea is to add a second RF mode at the third harmonic of the fundamental. Because significant field emission occurs only above a threshold field, the amplitudes of the modes can be selected to activate the emitter only once for each period of the fundamental, when the two waves interfere constructively and with the correct polarity to extract electrons. The result is a pulse that is short (determined by the period of the third harmonic), and the timing of which can be shifted over some range by changing the phase relationship between the modes (generally, beam dynamics are optimized by launching the bunch ahead of the crest of the field). A gun based on this concept could potentially use gated or ungated emitters.

Though not based on an RF gun, we mention here a current project at the Paul Scherrer Intitute that would use a field emission source coupled to an RF accelerator [33, 34]. The goal in this case is to develop an ultra low emittance source to drive an x-ray FEL. Both single tips and gated arrays with integrated focusing are being evaluated. The beam from the cathode will be accelerated across a 4 mm gap by a pulsed 1 MV voltage. From there, the beam enters an RF accelerator, where ballistic and magnetic bunch compression are used to produce the required bunch length.

1.7   FEAs and emittance: survey of the literature

Though limited in extent, there are some studies in the literature regarding the emittance of FEAs, mostly tied to their use in microwave tubes, and mostly

dealing with gated arrays. In this section, we will discuss several studies that are directly related to our work. For a broader sampling, see section 3.3.8 of [12] and section 4.4.1 of [18].

Liu and Lau [35] studied the emittance of a two-dimensional wedge shaped emitter. Approximating the cross section of the wedge by a Lorentzian function, they are able to restate the problem in a dimensionless form. The dimensionless trajectories are then solved numerically, leading to a general solution that can then be scaled based on the parameters of the problem.

Recently Jensen [15], in a significant extension to his earlier work [36], has developed a theory to determine the emittance of beams generated from structures of varying geometries. With analytic and numerical components, it is based on the "point charge model" [37], which gives a balance between accurate depiction of the emitter shape and computational efficiency. The point charge model has scaling properties that can be used to predict how altering the tip shape from a given baseline will affect the results [38, 15]. In the paper, comparisons are made between the theory and experimental results from the literature, and other topics related to the use of FEAs in accelerators (current density, switching frequency, effects of space charge) are discussed.

Two experimental studies are of particular interest. In 1992, Kirkpatrick *et al.* [39] measured the angular distribution of electrons emitted from ungated $TaSi_2$ rods. The diameter of the rods was 1 μm, and their heights ranged from 1–60 μm. Numerical calculations were also carried out to predict how the emittance would vary across a range of emitter sizes and operating voltages. More recently, Jarvis *et al.* [22, 40]

have measured the emittance of beams generated from ungated diamond pyramid FEAs. The results of these studies will be discussed in chapter 3.

For the general situation where multiple beamlets merge to form a single beam, Rhee and Boulais [41] have studied the way in which the characteristics of individual beamlets determine the emittance of the combined beam. As intuition would predict, for a large, dense, uniform array of the type we are considering, the emittance of the combined beam reflects the total area filled by the beamlets (including any empty space between them), and the velocity distribution is spatially uniform and equal to the velocity distribution of a single beamlet, reflecting the loss of correlation between position and velocity once the beamlets overlap.

1.8   Outline

The goal of this dissertation is to explore some of the issues most critical to predicting how a field emission cathode-based RF gun would perform. As discussed above, either gated or ungated FEAs could be considered for this application, and the design issues and mode of operation would be different between the two cases. Here, we limit the discussion to ungated cathodes.

In the second chapter, we describe the prolate spheroidal boss model of a field emitter tip. The main utility of this model is that it can be solved analytically by separation of variables. At the beginning of the chapter, the parameters associated with the model are defined. Next, the properties of the electrostatic solution are discussed. At the end of the chapter, we illustrate the effect of emitter shape on

field enhancement across the surface of the boss.

In chapter 3, an upper bound on the transverse momentum of an electron emitted from an ungated field emitter is derived. This in turn defines an upper bound on the intrinsic emittance of the FEA. We emphasize that the result is not specific to the geometry of the prolate spheroidal boss. In fact, only a few general conditions must be met for this upper bound to apply. In the next part of the chapter, theoretical and experimental studies of field emitter emittance from the literature are examined in relationship to each other and to the upper bound, and several trends are identified that are later investigated.

In chapter 4, numerical calculations based on the prolate spheroidal boss model are used to investigate the behaviors seen in chapter 3 and to otherwise develop a better understanding of the properties of the transverse velocity distribution of emission from an FEA cathode. More insight is gained into the relationship between emitter shape and the velocity distribution. Two hypothetical emitters are defined based on the requirements imposed by the RF gun, and for these examples, the evolution of the beam properties over the duration of the pulse (caused by the varying magnitude of the RF field) is described.

In chapter 5, the focus shifts to the temporal emission profile for an FEA in an RF field, and the connection between emission timing and the longitudinal dynamics of the electrons as they are accelerated in the cathode cell. As a consequence of the shape of the Fowler-Nordeim current-voltage relationship, the fraction of the RF period over which emission occurs is nearly independent of the characteristics of the emitter and the frequency of the cavity. It is shown that the RF gun can

be designed so that electron back bombardment does not occur, indicating that an FEA cathode gun may be able to produce high average beam current.

Chapter 6 covers several topics. The relationship between our theoretical results and other theoretical models is reconsidered, and the complementary aspects of the models are emphasized. Predictions of how FEA cathodes will perform in an RF gun are formulated based on comparisons to the proven RF gun cathodes. After that, new results we have obtained are enumerated, follow-on research topics are suggested, and some concluding remarks are made.

Chapter 2

Properties of the prolate spheroidal boss model of a field emitter

This chapter introduces the prolate spheroidal boss model of a field emitter. Its associated geometry is defined, and its electrostatic solution is given, as is the electric field at the surface, which is needed to calculate the field emission current distribution.

2.1   The prolate spheroidal boss and other emitter models

A number of simplified geometries have been employed in analytic studies of field emitter tips: concentric spheres [42], sphere on cone [43], floating sphere [44], hyperboloid [45, 46], paraboloid, Saturn model [47], *etc.* We will use one of the simpler models, the conducting prolate spheroidal boss on a conducting plane [48]. This surface, formed by rotating an ellipse around its major axis, is illustrated in figure 2.1. In this chapter, we will discuss the properties of the electrostatic solution of the prolate spheroidal boss in an external field applied perpendicular to the plane. These properties will be used in later chapters to examine the dynamics of electrons emitted from the surface of the boss. Because this is a greatly simplified representation of an actual physical structure, there are many limitations to how well it can be made to reflect the properties of real emitters. Some of the relevant limitations will be noted.
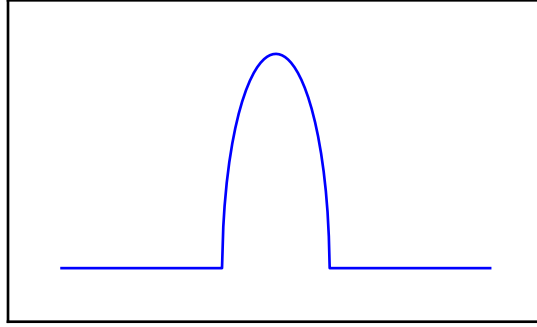
Figure 2.1: Cross section of a prolate spheroidal boss on a conducting plane.

The electrostatic solution for this problem can be solved in closed form by separation of variables in prolate spheroidal coordinates. The solution can then be transformed to Cartesian coordinates. It is therefore, for our purposes, not necessary to go into the details of the properties of spheroidal coordinate systems. Here, though, we define some of the parameters which describe the ellipses and hyperbolas that make up the spheroidal coordinate system, as they come up frequently in the results derived from the model.

2.2   Notation for the ellipse and hyperbola

Given a pair of focal points, an ellipse is defined as the set of all points such that the sum of the distances from each of the focal points to a given point on the ellipse is constant. Using the notation as defined in the figure 2.2, we have

$$d_t + d_b = k_e$$
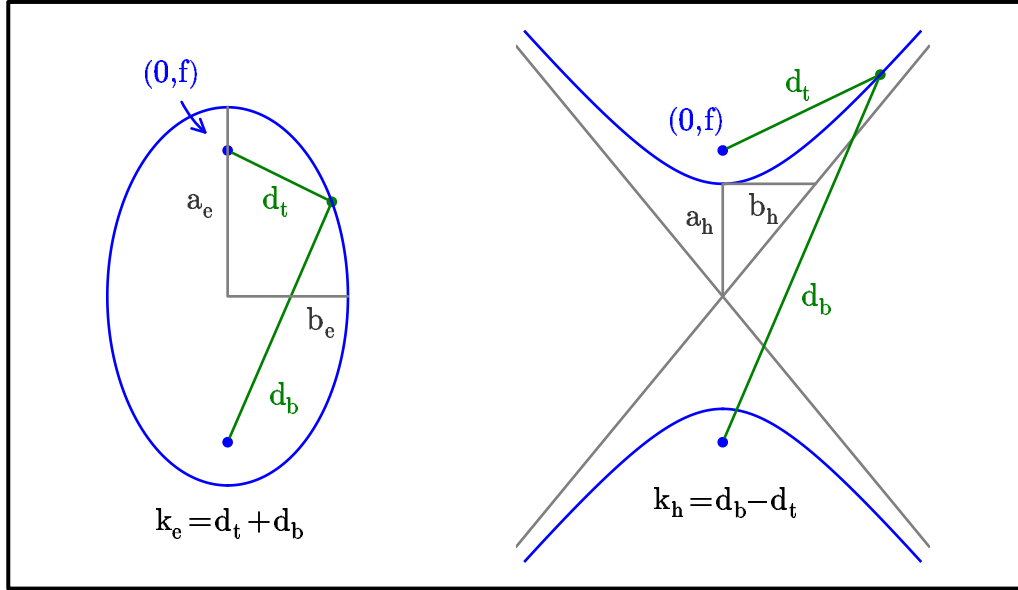
Figure 2.2: Geometry of the ellipse and hyperbola

where k_e is a constant. In terms of Cartesian coordinates, which we name r and z, this condition becomes

$$\sqrt{r^2 + (z - f)^2} + \sqrt{r^2 + (z - (-f))^2} = k_e.$$

The equation for the ellipse can be written alternately as

$$\frac{z^2}{a_e^2} + \frac{r^2}{b_e^2} = 1, \tag{2.1}$$

where a_e is the semimajor axis and b_e is the semiminor axis. These two forms are related in the following way [49]. As can be shown by comparing the two equations at the point where the ellipse crosses the major axis,

$$k_e = 2a_e. \tag{2.2}$$

By considering the point where the ellipse intersects the minor axis, it can be shown that $f^2 + b_e^2 = (k_e/2)^2$, so given $k_e = 2a_e$,

$$f^2 = a_e^2 - b_e^2. \tag{2.3}$$

The hyperbola is closely related to the ellipse. It is a set of points such that the difference between the distances from the two foci to a point on the hyperbola is constant. Using the notation from figure 2.2, the definition for the hyperbola is written

$$d_b - d_t = k_h,$$

or, in Cartesian coordinates,

$$\sqrt{r^2 + (z - (-f))^2} - \sqrt{r^2 + (z - f)^2} = k_h.$$

The equation for the hyperbola can also be written in the form

$$\frac{z^2}{a_h^2} - \frac{r^2}{b_h^2} = 1 \tag{2.4}$$

where again a_h is the semimajor axis and b_h is the semiminor axis. The semimajor axis is the height of the point where the hyperbola intersects the axis. Given a value for the semimajor axis, the semiminor axis sets the slope of the asymptotes. This can be seen by considering the behavior of equation 2.4 when r and z are large, where $z \approx (a_h/b_h)\, r$, as can be seen in figure 2.2.

The relationship between these two definitions of the hyperbola is as follows. By considering the point where the hyperbola intersects the major axis, it can be seen that $k_h = 2a_h$. Next, b_h can be related to f and k_h by comparing the asymptotic

29

forms of the two equations. The result is

$$b_h = \sqrt{f^2 - \left(\frac{k_h}{2}\right)^2}.$$

This is equivalent to the useful identity $f^2 = a_h^2 + b_h^2$.

2.3 Elliptic coordinate system

In three dimensions, the natural coordinate system for this problem is the prolate spheroidal coordinate system, which is formed by rotating an elliptic coordinate system around the major axis of its coordinate ellipses. Because the problem at hand has azimuthal symmetry, it reduces to a problem in two dimensional elliptic coordinates (also known as elliptic-cylindrical coordinates). An elliptic coordinate system is illustrated in figure 2.3. This coordinate system is comprised of confocal families of ellipses and hyperbolas. One difference between an elliptic coordinate system and more familiar ones is that its "shape" must be specified by giving the focal distance f. This focal distance supplies one of the parameters needed to locate the ellipse or hyperbola a point is located on, the other is given by specifying k_h or k_e. Unfortunately, there is no universal convention for how the coordinates are defined and named. We use the notation of Smythe [50], except we we use f for the distance from the origin to a focus (Smythe uses c_2). In this notation, the coordinates are defined as

$$\eta = \frac{k_e}{2f} = \frac{a_e}{f} = \frac{d_t + d_b}{2f} \tag{2.5}$$

$$\xi = \frac{k_h}{2f} = \frac{a_h}{f} = \frac{d_b - d_t}{2f}. \tag{2.6}$$
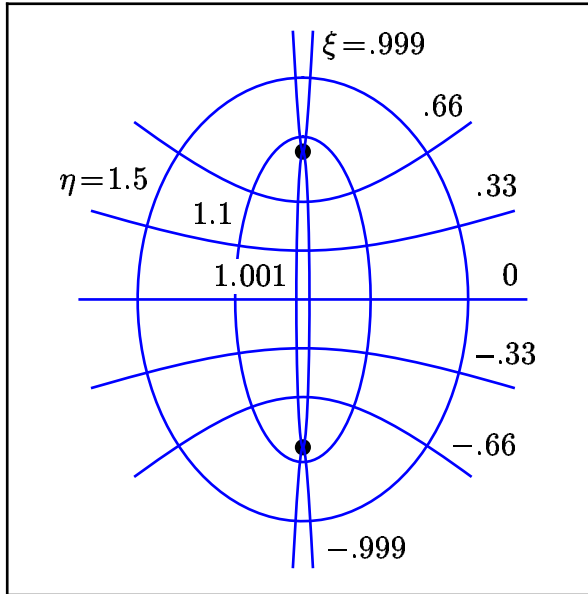
Figure 2.3: An elliptic coordinate system

The geometric significance of η and ξ is illustrated in figure 2.4. We note that $1/\eta$ is called the eccentricity of the ellipse; $1/\xi$ is the eccentricity of the hyperbola.

The inverse transformation, from elliptic coordinates into Cartesian coordinates, is

$$r = \frac{b_e b_h}{f} = f\sqrt{(1 - \xi^2)(\eta^2 - 1)} \qquad (2.7)$$

$$z = \frac{a_e a_h}{f} = f\eta\xi \qquad (2.8)$$

It is easily confirmed that substitution of these relationships into equations 2.1 and 2.4 yields the identities $a_e^2 - b_e^2 = f^2$ and $a_h^2 + b_h^2 = f^2$ respectively.

An alternate parameterization for the elliptical coordinates is formed with the
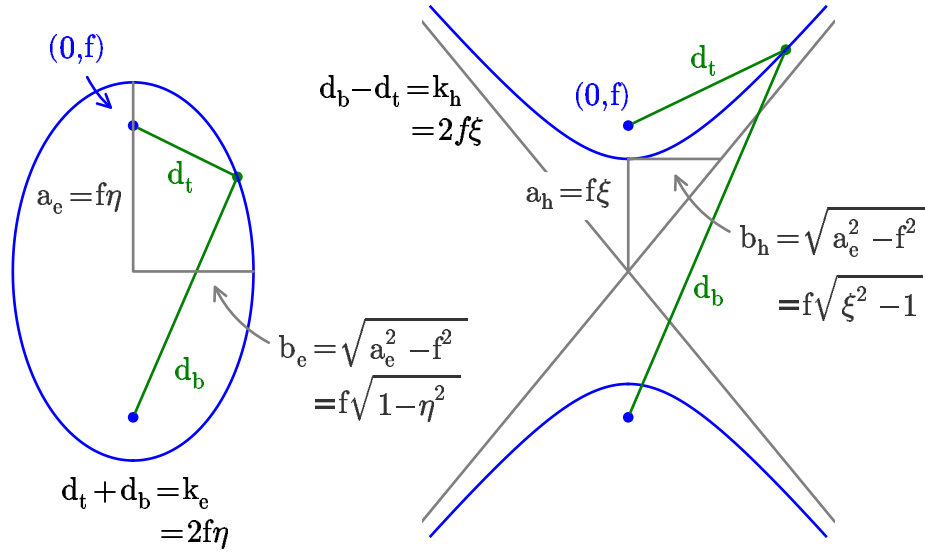
Figure 2.4: Definitions for η and ξ

substitutions [51]

$$\eta = \cosh\chi \qquad \text{and} \qquad \xi = \cos\theta$$

(where again, many combinations of symbols are in use). In this system, the transformation back to Cartesian coordinates (corresponding to equations 2.7 and 2.8) are

$$r = f\sinh\eta\sin\theta \qquad \text{and} \qquad z = f\cosh\eta\cos\theta \qquad (2.9)$$

$\theta = \text{acos}\,\xi$ is analogous to the angle coordinate in polar coordinates (ηf is similar to the radius). The coordinates defined by equations 2.3 can be convenient to use because the lines of constant θ are evenly distributed, as illustrated in figure 2.5.

A full description of elliptic and related coordinate systems can be found in many older textbooks. See, for example, chapter 5 of Morse and Feshbach [52].
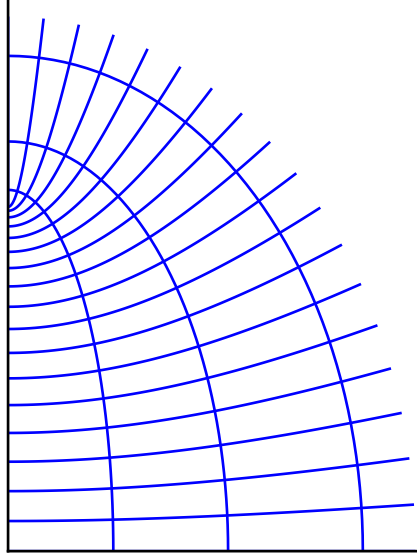
Figure 2.5: Alternate parameterization for an elliptic coordinate system. The ellipses are lines of constant χ; the hyperbolas are lines of constant θ. In particular, $\theta = \mathrm{acos}\,\xi$ is plotted every 5° between 0° (z axis) and 90° (r axis). We will often plot data as a function of this variable.

2.4 Electrostatic solution for the prolate spheroidal boss on a conducting plane

The electrostatic solution for the problem of the conducting prolate spheroidal boss on a conducting plane can be found, for instance, in the electrodynamics book by Smythe [50]. A somewhat more detailed version of the solution is provided in Kosmahl [53]. Little insight into the solution is gained by delving into the mechanics of separation of variables in elliptic coordinates, so we simply state the solution.

$$\Phi\left(\eta,\xi\right) = \mathrm{E_0 f_b}\, \mathrm{P}_1\left(\xi\right)\left[\mathrm{P}_1\left(\eta\right) - \frac{\mathrm{P}_1\left(\eta_b\right)}{\mathrm{Q}_1\left(\eta_b\right)}\, \mathrm{Q}_1\left(\eta\right)\right]$$

where P_1 and Q_1 are degree-one Legendre functions of the first and second type respectively. As we saw above, the η coordinate describes an ellipse; η_b is the

33
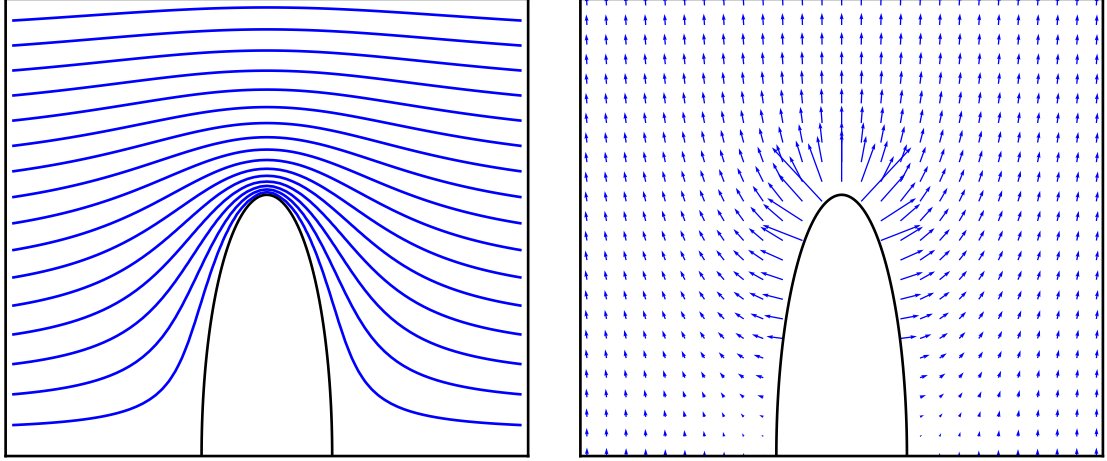
Figure 2.6: Electrostatic solution for the prolate spheroidal boss in a uniform applied field: equipotentials and electric field vectors.

value η takes on the surface of the boss. We see immediately the two terms in the brackets cancel when $\eta = \eta_b$ corresponding to the condition that the boss is grounded. It should be pointed out that the focal distance, which appears explicitly in this expression, also enters the equation implicitly through its appearance in the definitions of η and ξ. As mentioned above, this is one of the peculiarities of elliptical coordinate systems: the shape of the coordinate system itself must be chosen to fit the geometry of the problem. We have added the subscript "b" to emphasize that f_b is determined by the dimensions of the boss. If the emitter has height a_b and base radius b_b, $f_b = \sqrt{a_b^2 - b_b^2}$ by equation 2.3. Finally, $\eta_b = a_b/f_b$ as defined in equation 2.5.

Next, we use the definitions of the Legendre functions to restate the potential using more familiar functions.

$$ P_1(x) = x \qquad \text{and} \qquad Q_1(x) = \frac{1}{2}x \ln\left(\frac{x+1}{x-1}\right) - 1 = x \operatorname{acoth}(x) - 1. $$
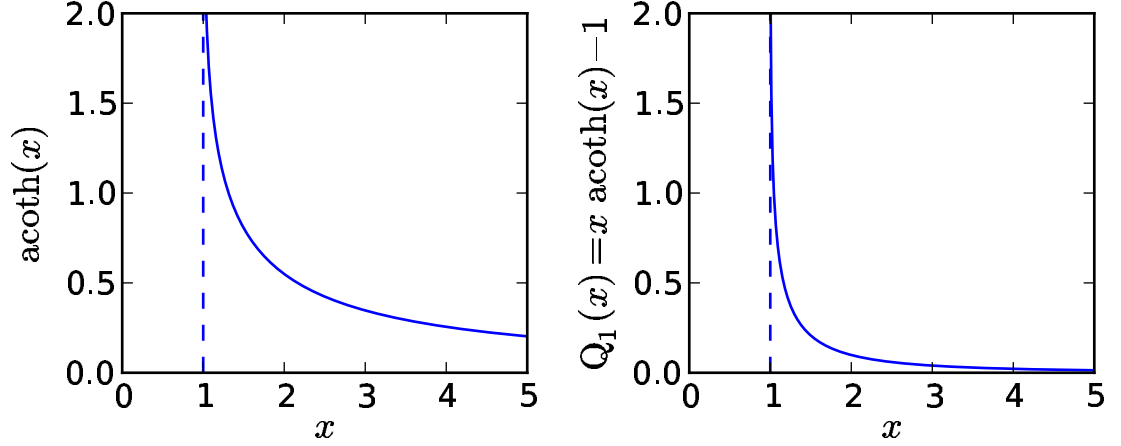
Figure 2.7: The functions $\mathrm{acoth}\,(x)$ and $Q_1(x)$

$\mathrm{acoth}\,(x)$ and $Q_1(x)$ are plotted in figure 2.9. the solution stated above becomes

$$\Phi\left(\eta, \xi\right) = E_0 f_b \xi \left[\eta - \eta_b \frac{\eta\,\mathrm{acoth}\,(\eta) - 1}{\eta_b\,\mathrm{acoth}\,(\eta_b) - 1}\right]. \tag{2.10}$$

On the $z = 0$ plane, $\xi = 0$ so $\Phi = 0$. Far above the emitter, η is large, causing the second term in the brackets to vanish, and we are left with $\Phi \approx E_0 f_b \eta \xi$. From equation 2.8 we have $f_b\,\xi\eta = z$, so $\Phi \approx E_0 z$ in accordance with the uniform applied field. Returning to the exact solution, rearranging terms and employing the relationship $f_b\,\xi\eta = z$, we end up with

$$\Phi\left(r, z\right) = E_0 z \left[1 - \frac{\dfrac{\eta\,\mathrm{acoth}\,(\eta) - 1}{\eta}}{\dfrac{\eta_b\,\mathrm{acoth}\,(\eta_b) - 1}{\eta_b}}\right] \tag{2.11}$$

with

$$\eta\left(r, z\right) = \frac{\sqrt{r^2 + (z - f_b)^2} + \sqrt{r^2 + (z + f_b)^2}}{2f_b}$$

where, summarizing from above,

$$f_b = \sqrt{a_b^2 - b_b^2} \qquad \text{and} \qquad \eta_b = \frac{a_b}{f_b} = \frac{a_b}{\sqrt{a_b^2 - b_b^2}}$$

where a_b is the height of the boss and b_b is the radius of the base.

2.5 Electric field at the surface of the boss

Kirkpatrick studied the effective emission area (the area factor) for sharp tips by integrating the distribution of field emission across the surface of a prolate spheroidal boss [48]. Later, in order to calculate velocity distributions, we will need to know this emission distribution. We describe it here.

Because the surface of the boss is a surface of constant η, the normal vector is in the direction of the unit vector $\hat{\eta}$. The electric field is

$$\mathbf{E} = -\nabla\Phi$$

so the magnitude of the surface field is

$$\mathrm{E}_{\eta_0} = [-\hat{\eta} \cdot \nabla\Phi]_{\eta=\eta_{\mathrm{b}}} \, .$$

The general expression for the gradient operator in curvilinear coordinates as well as the scale factors for elliptic coordinates can be found, for instance, in Morse and Feshbach [52] (sections 1.4 and 5.1 respectively):

$$\nabla\Phi = \frac{1}{h_1}\frac{\partial\Phi}{\partial\omega_1}\hat{\mathbf{a}}_1 + \frac{1}{h_2}\frac{\partial\Phi}{\partial\omega_2}\hat{\mathbf{a}}_2$$

$$\omega_1 = \eta, \quad h_1 = h_\eta = f\sqrt{\frac{\eta^2-\xi^2}{\eta^2-1}} \quad \text{and} \quad \hat{\mathbf{a}}_1 = \hat{\eta}$$

$$\omega_2 = \xi, \quad h_2 = h_\xi = f\sqrt{\frac{\eta^2-\xi^2}{1-\xi^2}} \quad \text{and} \quad \hat{\mathbf{a}}_2 = \hat{\xi}.$$

For our η they use μ in their notation, and, confusingly, our ξ is their η. Our f is their d. The gradient in elliptic coordinates is therefore

$$\nabla\Phi = \frac{1}{f}\sqrt{\frac{\eta^2-1}{\eta^2-\xi^2}}\frac{\partial\Phi}{\partial\eta}\,\hat{\eta} + \frac{1}{f}\sqrt{\frac{1-\xi^2}{\eta^2-\xi^2}}\frac{\partial\Phi}{\partial\xi}\,\hat{\xi}$$

so the quantity we seek

$$\mathrm{E}_{\eta_0} = [-\hat{\eta} \cdot \nabla \Phi]_{\eta=\eta_\mathrm{b}} = \left[-\frac{1}{\mathrm{f}_\mathrm{b}} \sqrt{\frac{\eta^2 - 1}{\eta^2 - \xi^2}} \frac{\partial \Phi}{\partial \eta} \right]_{\eta=\eta_\mathrm{b}}$$

where, from equation 2.10, we find

$$\frac{\partial \Phi}{\partial \eta} = \mathrm{E}_0 \mathrm{f}_\mathrm{b} \xi \left[\frac{\eta_\mathrm{b}}{\eta_\mathrm{b} \operatorname{acoth}(\eta_\mathrm{b}) - 1} \frac{1}{\eta(\eta^2 - 1)} + \left(1 - \frac{\frac{\eta \operatorname{acoth}(\eta) - 1}{\eta}}{\frac{\eta_\mathrm{b} \operatorname{acoth}(\eta_\mathrm{b}) - 1}{\eta_\mathrm{b}}} \right) \right].$$

At $\eta = \eta_\mathrm{b}$, the second term is zero, leaving

$$\left[\frac{\partial \Phi}{\partial \eta} \right]_{\eta=\eta_\mathrm{b}} = \mathrm{E}_0 \mathrm{f}_\mathrm{b} \xi \frac{1}{(\eta_\mathrm{b}^2 - 1)} \frac{1}{\eta_\mathrm{b} \operatorname{acoth}(\eta_\mathrm{b}) - 1},$$

and the final result is

$$\mathrm{E}_{\eta_0} = -\mathrm{E}_0 \frac{1}{\eta_\mathrm{b} \operatorname{acoth}(\eta_\mathrm{b}) - 1} \frac{\xi}{\sqrt{(\eta_\mathrm{b}^2 - 1)(\eta_\mathrm{b}^2 - \xi^2)}}. \tag{2.12}$$

The maximum field enhancement, $\beta = \mathrm{E}_{\eta_0} / (-\mathrm{E}_0)$ occurs at the apex of the boss, where $\xi = 1$, giving

$$\beta(\eta_\mathrm{b}) = \frac{1}{(\eta_\mathrm{b}^2 - 1)(\eta_\mathrm{b} \operatorname{acoth}(\eta_\mathrm{b}) - 1)}.$$

As a caution, the field enhancement factor for gated FEAs is usually defined instead as the ratio of apex field to gate voltage.

2.6   Curvature of the tip and field enhancement

In most cases, the characteristic of an emitter with the strongest influence on field enhancement is the radius of curvature of the tip (see, for example, section 4.3.1 of [18]), which we will call c_r. The radius of curvature of the tip can be determined by finding a sphere of radius c_r, centered at $a_\mathrm{b} - c_r$, whose contour matches that

of the boss near the apex. This configuration is illustrated in figure 2.8. The cross sections of the two structures are given by
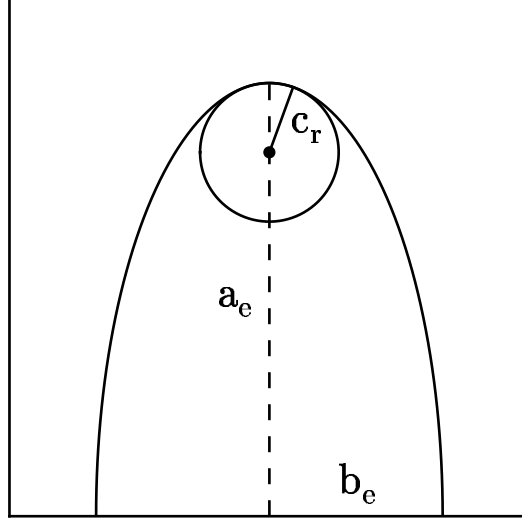
Figure 2.8: A circle whose radius of curvature equals that of the tip of the ellipse

$$\text{ellipse:} \quad \frac{z^2}{a_e^2} + \frac{r^2}{b_e^2} = 1 \qquad\qquad \text{circle:} \quad r^2 + (z - (a_b - c_r))^2 = c_r^2$$

Expressed as functions of z, these equations become

$$z_e = a_b\sqrt{1 - \left(\frac{r}{b_b}\right)^2} \qquad\qquad z_c = c_r\sqrt{1 - \left(\frac{r}{c_r}\right)^2} + a_b - c_r.$$

Near the apex, r is small compared to both b_b and c_r, so we can use approximation based on the Taylor series expansion for $\sqrt{1+x}$ at $x = 0$, $\sqrt{1+x} \approx 1 + \frac{1}{2}x$, to rewrite the equations as

$$z_e \approx a_b\left[1 - \frac{1}{2}\left(\frac{r}{b_b}\right)^2\right] \qquad\qquad z_c \approx c_r\left[1 - \frac{1}{2}\left(\frac{r}{c_r}\right)^2\right] + a_b - c_r.$$

or

$$z_e \approx a_b - \frac{1}{2}\frac{a_b r^2}{b_b^2} \qquad\qquad z_c \approx a_b - \frac{1}{2}\frac{r^2}{c_r}$$

which are equivalent when

$$c_r = \frac{b_b^2}{a_b}.$$ (2.13)

In figure 2.9, we plot field enhancement factors for bosses with $f_b = .5$ μm and $c_r = 5$, 25, and 100 nm. Most microfabricated emitters have $c_r < 100$ nm. Spindt cathodes generally fall in the range of 10-50 nm, while silicon emitters can have $c_r < 10$ nm (see section 1.5.4 for references). The diamond pyramid FEAs we have emphasized have $c_r = 20$ nm [21]. The figure is not exactly representative of these examples because height and other features of their geometry will also affect field enhancement, but it correctly illustrates the general trend.
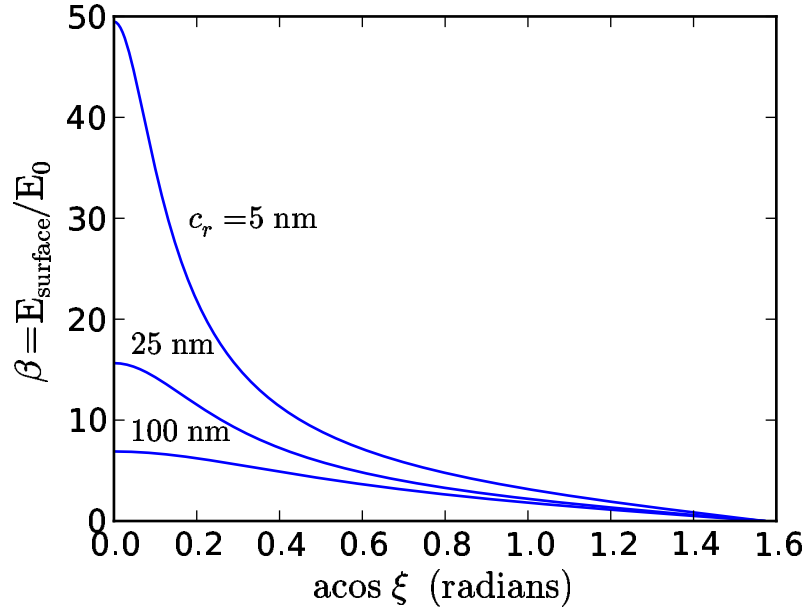
Figure 2.9: Field enhancement for three prolate spheroids with $f_b = .5$ μm. For the emitter with $c_r = 5$ nm, $a_b = .503$ μm, $a_b = .05$ μm, and $\eta_b = 1.005$. For the emitter with $c_r = 25$ nm, $a_b = .51$ μm, $a_b = .11$ μm, and $\eta_b = 1.025$. Finally, for the emitter with $c_r = 100$ nm, $a_b = .55$ μm, $a_b = .24$ μm, and $\eta_b = 1.105$. See figure 2.5 for a depiction of the coordinate $\theta = \mathrm{acos}\,\xi$.

Chapter 3

An upper limit on transverse momentum for electrons emitted from
an ungated field emitter

In the first chapter, we described the importance of emittance as a measure
of beam quality. In this chapter, we will show that it is possible to determine an
upper bound on the emittance of an ungated field emitter.

In section 1.4.3, it was shown how the intrinsic emittance of a thermionic
cathode is determined. Because, at the source, there was no correlation between
electron position and velocity, the intrinsic emittance was the product of the rms
spatial distribution of the electrons and the rms velocity distribution. For an FEA,
a similar condition holds. Though position and velocity *are* correlated in close
proximity to each tip, the beamlets rapidly merge, and the correlation is lost. A
detailed study of the emittance of beams formed by the merger of multiple beamlets
was conducted by Rhee and Boulais [41], but for a dense, uniform array of sources,
the correlation is negligible, and the emittance of the array can be calculated in the
same way it was for the thermionic cathode.

The problem of calculating the intrinsic emittance of an FEA is therefore
reduced to calculating the velocity distribution of the electrons emitted from a single
tip. Determining the velocity distribution accurately requires both the distribution
of emission across the tip and the final transverse momentum of the electrons as

a function of point of emission to be know. This approach has been taken as the foundation for studies combining analytical and computational methods [15, 35]. Below, we will show that an upper bound on the transverse momentum, and hence intrinsic emittance, can be found analytically. This result will complement the more exact methods.

Qualitatively speaking, electrons emitted away from the apex of a tip receive a transverse momentum kick due to the strongly distorted fields in the close vicinity of the tip. Because the magnitude of the field is large and the energy of the electrons is small, their trajectories closely follow the field lines [15]. Conversely, farther from the emitter, the field lines flatten out and the electrons have greater momentum, so the potential for transverse momentum gain diminishes rapidly. Electrons emitted near the apex experience little transverse acceleration, but because emittance is an rms measure, trajectories that accumulate greater transverse momentum receive greater weighting. Ultimately, it is the distribution of emission across the tip that determines how close the true emittance is to the upper bound. No general rule will be given to quantify this dependence, but comparisons will be made to experimental results and numerical examples will be presented that will give some indication of the relationship.

3.1   Simplifying approximations

In the analysis that follows, we will make two simplifying approximations when considering the effects of the tips on the trajectories: first, that relativistic effects

can be ignored, and second, that the RF field can be approximated as a static field Here, we discuss the validity of these approximations.

The degree to which relativistic effects are important can be determined by comparing the electron's kinetic energy to the energy corresponding to its rest mass. The peak accelerating fields achievable in an RF gun are on the order of 100 MV/m, or 100 V/μm. Typical field emitter tips are one to a few microns tall, so, at a distance of ten times the emitter height from the cathode, the kinetic energy of the electron can not be much greater than several thousand electron volts, compared to an electron rest mass of 511 keV. Therefore, relativistic effects can safely be neglected.

To show that the time dependence of the field can be neglected, we make the a priori assumption that this is the case, then demonstrate that the assumption has lead to a reasonable result. For non-relativistic acceleration, the trajectory of the particle in the field uniform field E_z is

$$z = \frac{eE_z}{2m}t^2 \qquad \text{or} \qquad t = \sqrt{\frac{2m}{eE_z}}z.$$

Emission occurs only when the accelerating field is near its maximum. Even if the field drops as low as 10 MV/m during this initial period of acceleration, the electron takes no more than 7.5 ps to travel 50 μm, where it is far from the region where the field is distorted by the FEA. The maximum rate at which the field changes occurs at the zero crossing, where

$$\frac{d}{dt}\left[E\left(t\right)\right]_{t=0} = \frac{d}{dt}\left[E_0 \sin\left(\omega_{RF}t\right)\right]_{t=0} = \omega_{RF}E_0 \quad \text{or} \quad \frac{d}{dt}\left[E\left(t\right)\right]_{t=0} = 2\pi\frac{E_0}{\tau_{RF}}.$$

For accelerators, 2.85 GHz is the highest frequency in common use. At that fre-

quency, $\tau_{\text{RF}} = 351$ ps. 7.5 ps thus corresponds to 2% of the RF period. The maximum the field can change during this time is $(dE/dt)\,\Delta t = 2\pi E_0 \times 2\%$ or about 12% of the peak field. The actual change will be significantly less because of the fact that emission occurs near the crest where the field is changing less rapidly. The error introduced by neglecting the changing field will be negligible in the context of the level of accuracy we hope to achieve.

3.2   Calculating the upper bound

If the force acting on a particle as a function of time is known, the change in the particle's momentum caused by the force can be calculated using Newton's second law. Here, the electric field is known, so the force is known as a function of position, but the connection between position and time is only known once the equations of motion have been solved. As is generally the case, the equations of motion for this problem are a coupled set of differential equations with no apparent closed-form solution. We are therefore led to seek an approximate solution. We will now show that a upper bound for the transverse component of the momentum can be found.

A useful relationship between force as a function of position and transverse momentum gain can be found in analogy with the derivation of the equivalence between work done on a particle and the change in its kinetic energy from Newton's second law in one dimension. Specifically, we consider the following series of steps.

Recasting

$$\mathrm{F} = \frac{dp}{dt} \quad \text{as} \quad \mathrm{F} = \frac{dp}{dx}\frac{dx}{dt} \quad \text{and using} \quad \frac{dx}{dt} = v = \frac{1}{\mathrm{m}}p$$

leads to

$$\mathrm{F} = \frac{dp}{dx}\left(\frac{1}{\mathrm{m}}p\right), \quad \text{or} \quad \frac{1}{\mathrm{m}}pdp = \mathrm{F}dx.$$

Integrating along a section of the particle's trajectory of the particle starting at the point x_I and ending at the point x_F,

$$\int_{p_I}^{p_F} \frac{1}{\mathrm{m}}pdp = \int_{x_I}^{x_F} \mathrm{F}(x)dx \quad \text{or} \quad \frac{p_F^2}{2m} - \frac{p_I^2}{2m} = \int_{x_I}^{x_F} \mathrm{F}(x)dx;$$

the work done on the particle results in an equivalent change in the particle's kinetic energy. Although this derivation ostensibly applies to motion in one dimension, we note that the mathematics behind it applies equally well to the motion in each individual dimension of a multidimensional Cartesian coordinate system. Of particular interest for the case at hand,

$$\frac{p_{r,F}^2}{2m} - \frac{p_{r,I}^2}{2m} = \int_{r_I}^{r_F} \mathrm{F}_{\mathrm{r}}(r, z(r))dr$$

where F_r is the $\hat{r}$ (transverse) component of the force. We write z as $z(r)$ to emphasize that we are considering this a problem in the single dimension r, although the dependence of z on r remains an unknown. Because the equipotentials wrap around the emitter, the field vector's transverse component is always directed outward, at least for any reasonably simple emitter geometry. Because the electron is always being pushed away from the axis, an increase in z will always be accompanied by an increase in r, so we are justified to say z is a function of r.

We will now show that, although we do not know $z(r)$ and consequently do not know F_{r}, we can set an upper bound on F_{r} at each point r. If F_{r} is always positive,

as we have just argued is reasonable to assume, the upper bound of the integral is simply the integral of the upper bound at each point. This, in turn, leads to an upper bound on the accumulated transverse momentum.

The condition we assume which leads to an upper bound on $F_r(r, z)$ is that, for fixed r, $F_r(r, z)$ decreases with increasing z. In other words, no matter what the actual value of z is when the trajectory reaches a certain r, the true value of F_r seen by the electron is less than $F_r(r, z_0)$. This is true for the prolate spheroidal boss model, and it seems likely to hold for similarly simple, pointed geometries, but it would need to be verified for each case.

We consider an electron emitted from a point (r_0, z_0) on the surface of the boss. Field-emitted electrons are, in most cases, emitted with very low kinetic energy [54]. We assume this initial energy can be neglected, and set $p_{r,I} = 0$, so

$$\text{U.B.}\left[\frac{p_r^2}{2m}\right] = \int_{r_0}^{\infty} F_r(r, z_0) dr.$$

The integral is recognized as the work that must be done to move an electron from the point where it is emitted to $r = \infty$ along a line in the $z = z_0$ plane, which is equal to the difference between the potential at the emission point and the point $(r = \infty, z_0)$:

$$\text{U.B.}\left[\frac{p_r^2}{2m}\right] = \Phi(r = \infty, z_0) - \Phi(r_0, z_0).$$

The emitter is grounded, so $\Phi(r_0, z_0) = 0$. $\Phi(r = \infty, z_0)$, far from the distortions induced by the boss, is $eE_0 z_0$, so we are simply left with

$$\text{U.B.}\left[\frac{p_r^2}{2m}\right] = eE_0 z_0.$$

45

The upper bound on the transverse velocity is now

$$\text{U.B.}[\,v_r\,] = \sqrt{2\frac{e\mathrm{E}_0 z_0}{\mathrm{m}}}. \tag{3.1}$$

If emission is radially isotropic, the upper bound on the rms value of either Cartesian component of the velocity vector is

$$
\begin{aligned}
\text{U.B.}[\,\tilde{v}_x\,] &= \sqrt{\frac{\displaystyle\int_{-\frac{\pi}{2}}^{\frac{\pi}{2}} (\text{U.B.}[\,v_r\,]\times\cos\phi)^2\,d\phi}{\displaystyle\int_{-\frac{\pi}{2}}^{\frac{\pi}{2}} d\phi}} = \text{U.B.}[\,v_r\,]\sqrt{\frac{\displaystyle\int_{-\frac{\pi}{2}}^{\frac{\pi}{2}} \cos^2\phi\,d\phi}{\displaystyle\int_{-\frac{\pi}{2}}^{\frac{\pi}{2}} d\phi}} \\
&= \frac{1}{\sqrt{2}}\,\text{U.B.}[\,v_r\,] \\
&= \sqrt{\frac{e\mathrm{E}_0 z_0}{\mathrm{m}}}. \tag{3.2}
\end{aligned}
$$

By equation 1.5, the upper bound on the source (normalized intrinsic) rms emittance is $\tilde{x}\,\tilde{v}_x/\mathrm{c}$, so

$$\text{U.B.}[\,\tilde{\epsilon}_{s,x}\,] = \tilde{x}\,\sqrt{\frac{e\mathrm{E}_0 z_0}{\mathrm{mc}^2}}$$

and if the emitters are uniformly distributed on a circular cathode of radius a, $\tilde{x} = a/2$, therefore

$$\text{U.B.}[\,\tilde{\epsilon}_{s,x}\,] = \frac{a}{2}\,\sqrt{\frac{e\mathrm{E}_0 z_0}{\mathrm{mc}^2}}.$$

We see then, from equation 1.6, the emittance of an FEA source can be *no more than* that of a thermionic cathode at temperature $\mathrm{kT} = e\mathrm{E}_0 z_0$. Because this is an upper bound, we do not immediately make comparisons to the intrinsic emittance of other cathode types. In the following section, we will begin to consider typical FEA emittance values, an investigation that is continued in chapter 5. The relative performance of different cathode types will be discussed in chapter 6.

3.3 Comparison with experiments

We begin by considering the experimental measurements on DFEA structures conducted by the group at Vanderbilt University. In their most recently reported experiments [22], electrons are extracted from diamond pyramids with a height of .75 μm (inferred from figure 6 of [40]) by a 1.3 kV potential applied across a 1.3 kV gap ($E_0 = 5.7$ MV/m). The measured rms angular beam divergence in x, corrected for the defocusing effect of the pepperpot aperture, was $\tilde{\theta}_x = 46$ mrad. For a 1.3 keV electron, $v_0 = 2.1 \times 10^7$ m/s, so $\tilde{v}_x = \tilde{\theta}_x v_0 = 9.8 \times 10^5$ m/s.

For $z_0 = .75$ μm and $E_0 = 5.7$ MV/m, equation 3.1 predicts an upper bound on the transverse velocity of U.B.$[\,v_r\,] = 1.2 \times 10^6$ m/s, and equation 3.2 predicts an upper bound on the rms x component of the transverse velocity of U.B.$[\,\tilde{v}_x\,] = 8.7 \times 10^5$ m/s when the emission distribution is symmetric around the axis. Because the pyramids are not radially symmetric, the fact that this second limit is exceeded is not a contradiction. Still, other examples we will examine do not fall as close to the upper bound. One possible explanation is that space charge forces, which would tend to expand the beamlet, are non-negligible. Another observation is that the FWHM intrinsic energy spread of the electrons, measured in separate experiments [55], was found to be approximately 1.3 eV. This value, which is higher than that seen for field emission from most materials, is not negligible compared to the effective temperature of the transverse distribution implied by the relationship $\tilde{v}_x = \sqrt{kT/m}$, which is kT = 5.5 eV in this case. Finally, it is possible that the conditions imposed in the derivation of the upper bound are not met for this geometry.

A second comparison to experiment can be made with the results of Kirkpatrick *et al.* for TaSi$_2$ rod emitters. The emitters that were tested were exceptionally tall and narrow, with diameters of roughly 1 μm and heights ranging from 20–60 μm. A triangle wave pulse with a peak voltage of 10 kV was applied across a roughly 1 mm gap to extract the current, corresponding to a peak E$_0$ of 10 MV/m. The divergence of the envelope of a beamlet originating from a small aperture was found to be 30 mrad. At 10 keV, $v_0 = 5.8 \times 10^7$ m/s, so $\tilde{v}_x = \tilde{\theta}_x v_0 = 1.8 \times 10^6$ m/s. Depending on the distribution of tip heights, the predicted upper bound would fall between the value for the shorter tips in the array ($h = 20$ μm), which is U.B.$[\tilde{v}_x] = 5.9 \times 10^6$, or 3.3 times the measured value, and that for the 60 μm tips, which is $\sqrt{3}$ times higher.

3.4 Comparison to other theories

There is a connection between the upper bound determined above and Liu and Lau's [35] calculations for the two-dimensional wedge. For the average of the normalized divergence, they find

$$\overline{\gamma\beta\theta} = 0.0442 \, \overline{V}_x\!\left(\epsilon, \overline{b}\right) \left[\left(\frac{\mathrm{E}_0}{10^9 \text{ V/m}}\right)\left(\frac{h}{1 \text{ } \mu\text{m}}\right)\right]^{1/2} \quad \text{(Liu and Lau)}$$

where h is the emitter height (our z_0) and $\overline{V}_x\!\left(\epsilon, \overline{b}\right)$ is a dimensionless, numerically calculated parameter with a maximum value of .5 that describes the average properties of the velocity distribution. To compare this result to ours, we state it in the low energy (unnormalized) form, $\overline{\gamma\beta\theta} \approx \overline{\beta\theta} = \overline{v}_x/c$, in other words, we must multiply $\overline{\gamma\beta\theta}$ by c to state the result as an average velocity. Combining the numerical

48

terms leaves $\overline{v}_x = 4.2 \times 10^5 \, \overline{V}_x\left(\epsilon, \overline{b}\right) \sqrt{\mathrm{E}_0 h}$. This equation should be compared to our

equation 3.1 for U.B.$[\,\tilde{v}_r\,]$ instead of the one for U.B.$[\,\tilde{v}_x\,]$ because the equation for

U.B.$[\,\tilde{v}_x\,]$ is corrected for the radial distribution of the velocity vectors, which does

not apply in the case of the wedge where there is only one transverse coordinate.

In numerical terms, equation 3.1 is U.B.$[\,\tilde{v}_r\,] = 5.9 \times 10^5 \sqrt{\mathrm{E}_0 z_0}$. Because Liu and

Lau's expression is for the *average* velocity, we have not shown that their result falls

below the upper bound. It does, however, illustrate the relationship between the

upper bound and a more detailed calculation.

Because Jensen's method [15] is a very flexible approach, it is more challenging

to elucidate the relationships that may exist between it and this work. Further

investigation will be required to determine any possible connections.

3.5   Comments

The upper bounds that were determined do not give any indication of what

effect the aspect ratio of the emitter has on the trajectories. In the next chapter,

we will calculate the exact solution numerically for several sets of conditions to see

what role aspect ratio plays. We will then discuss, qualitatively, how the results

would be expected to change for a real emitter shape as opposed to the idealized

geometry of the prolate spheroidal boss.

The transverse velocity distribution is determined by convolving the trans-

verse velocity of a particle emitted from a given point on the emitter surface with

the distribution of current density across the surface. Like the trajectories, the

current density is determined by the emitter shape and applied field, a topic we will address in the next chapter. Generally, though, the analysis presented in this chapter suggests that a stronger field near the emitter surface, whether achieved by increasing the applied field or by increasing the height of the emitter, leads to greater transverse momentum gain for electrons emitted off-axis, and thus would suggest increased emittance. This was the conclusion reached by Liu and Lau [35] in their investigation of the two-dimensional wedge. They further observed that higher field would lead not just to higher emittance but also to higher current, so the brightness could be increased or decreased depending on how the competing effects balance out.

Chapter 4

Numerical calculations based on the prolate spheroidal boss model

For a field emission cathode, the transverse velocity distribution, and hence the emittance, is determined by the convolution of the emission distribution with the distribution of final transverse velocities for the trajectories. The emission distribution effectively determines how close the actual emittance is to the upper bound determined in the previous chapter. In this chapter, we will use numerical examples to examine the relationship between the role of the emission distribution and the trajectory properties in determining the velocity distribution. The implementation of the calculations is described in appendix A.

Because azimuthal symmetry is assumed, for a given boss shape, each trajectory is uniquely defined by a single parameter: the distance between the apex and the emission point. The characteristic of the trajectories which is of interest to us is the final transverse velocity. We will label the distribution of final transverse velocities as a function of emission location the v_r–ξ distribution. v_x–ξ will represent the analogous relationship for the x component of the transverse velocities.

For the calculations, the prolate spheroidal boss model will be used. This model is simple to implement, and it narrows the otherwise vast parameter space. In reality, it is too simple to model almost any real emitter with accuracy, first and foremost because the tip shape of a prolate spheroid is tied directly to its

macroscopic dimensions, and in practice small changes to the shape of the tip can significantly impact the emission distribution. To account for these effects, a more sophisticated model (such as the point charge model [15]) or exact calculations using a beam code are required. Nevertheless, for our purpose, which is primarily to gain greater insight into the results from the previous chapter, the prolate spheroidal boss model is sufficient. In some cases, the aspect ratios are greater than those seen with common emitter types. These examples are used to illustrate the characteristics of very sharp tips, which could not otherwise be represented with this model.

We start the chapter by considering the impact of emitter shape on the trajectories. Then, two sample emitter parameter sets are defined, each related to a specific hypothetical operating point for an RF gun. For these emitters, the emission distribution and v_r–ξ distribution are calculated and plotted for several values of applied field. Finally, the rms x component of the transverse velocity ($\tilde{v}_x$) is plotted as a function of applied field. This data is found to imply a modest variation in emittance over the duration of the pulse when an RF extraction field is used.

4.1   Relationship between transverse velocity and emission location

In this section, examples of the influence of emitter shape on the v_r–ξ relationship are given. To give a qualitative indication of how the trajectories behave, trajectories are plotted for two emitter shapes in figure 4.1. Close to the tip, the field is strong and the inertia of the electrons is low, so the trajectories closely follow the field lines [15].
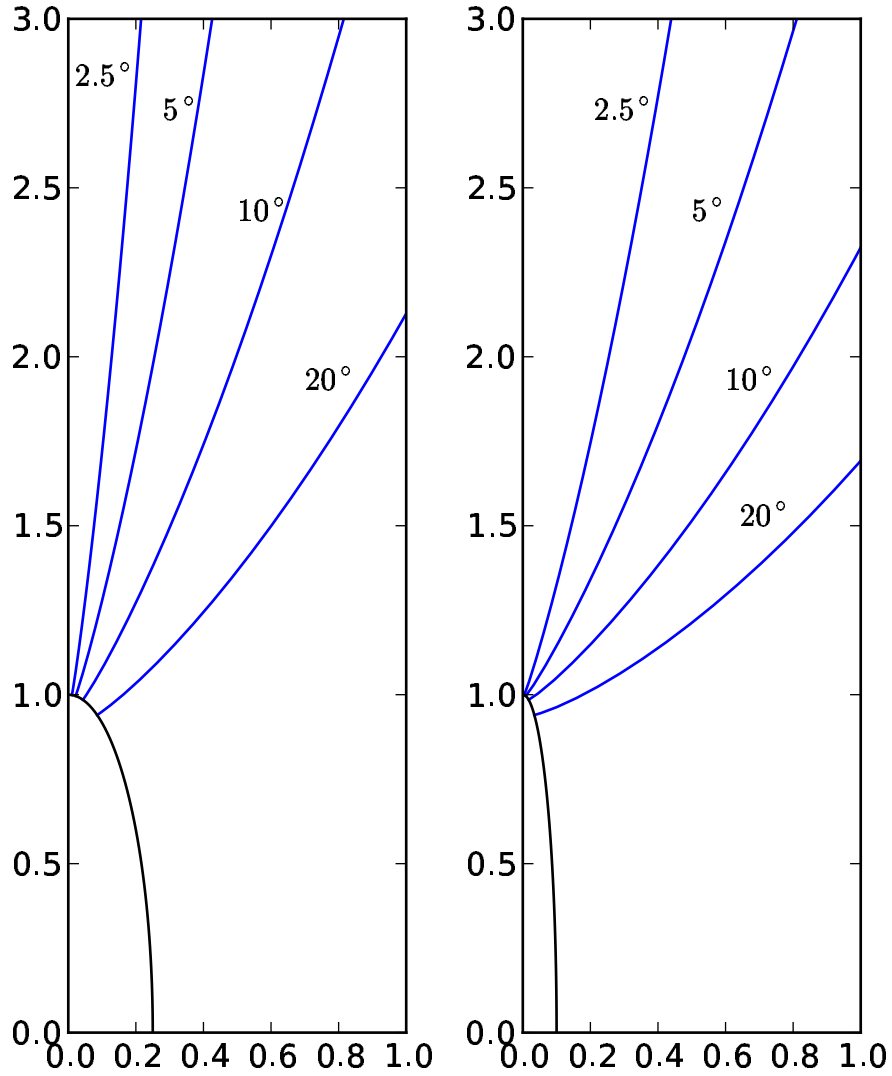
Figure 4.1: Trajectories of electrons emitted from different points on a prolate spheroidal boss. The launch "angle" corresponds to acos ξ. The boss on the left has a height of 1 μm and a base radius of .25 μm. The emitter on the right has a height of 1 μm and a base radius of .1 μm. The applied field in both cases is 50 MV/m. The electrons have little inertia relative to the strength of the field, so they follow the field lines closely.

Because the upper bound on transverse momentum from the previous chapter gives no indication of the effect base radius has on the trajectories, we begin our discussion there. Figure 4.2 illustrates this dependence for two emitter heights. It is seen that reducing the base radius relative to the height causes the final velocities of the trajectories to converge with the upper bound more rapidly as the point of emission moves away from the apex. An initial consideration of this plot might imply that reducing the base radius leads to increased emittance values, but, at least for the prolate spheroidal boss, narrowing the base results in a smaller radius of curvature for the tip, which, as we will see below, confines the emission to a smaller area near the apex. These two trends have opposite effects. The experimental and theoretical results discussed at the end of the previous chapter reinforce the fact that there is not a direct connection between aspect ratio and the intrinsic emittance of the cathode.

Varying the emitter height (figure 4.3) or the applied field (figure 4.4) have little effect on the shape of the v_r–ξ relationship. Furthermore, the transverse velocities are seen to scale in nearly direct proportion to the upper bound. The upper bound was found to have a square root dependence on both emitter height and applied field, so the transverse velocity curves will have roughly that dependence. This dependence for the applied field follows from the fact that the electrons follow the field lines. Because the field lines are determined only by the geometry, the shape of the trajectories do not change in this case.
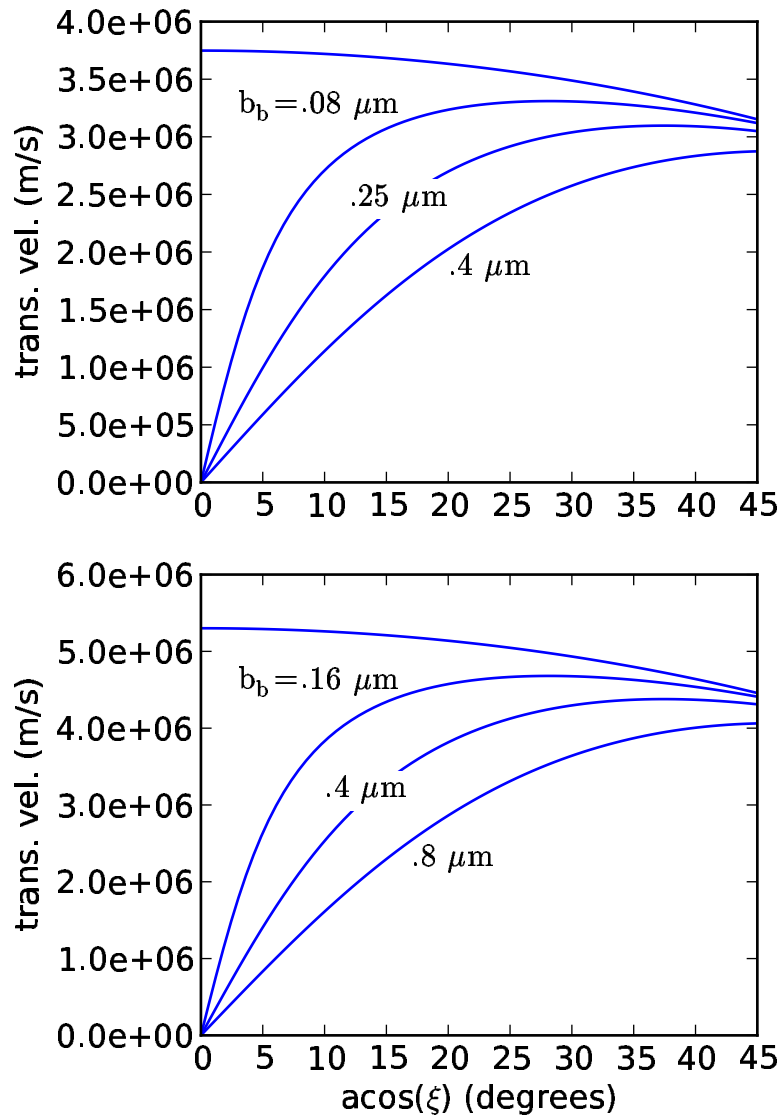
Figure 4.2: Effect of base radius on the trajectories for two emitter heights. The corresponding upper bound (see equation 3.1) is also plotted The emitter height is .8 μm in the top figure and 1.6 μm in the bottom figure. For both cases, the applied field is 50 MV/m.
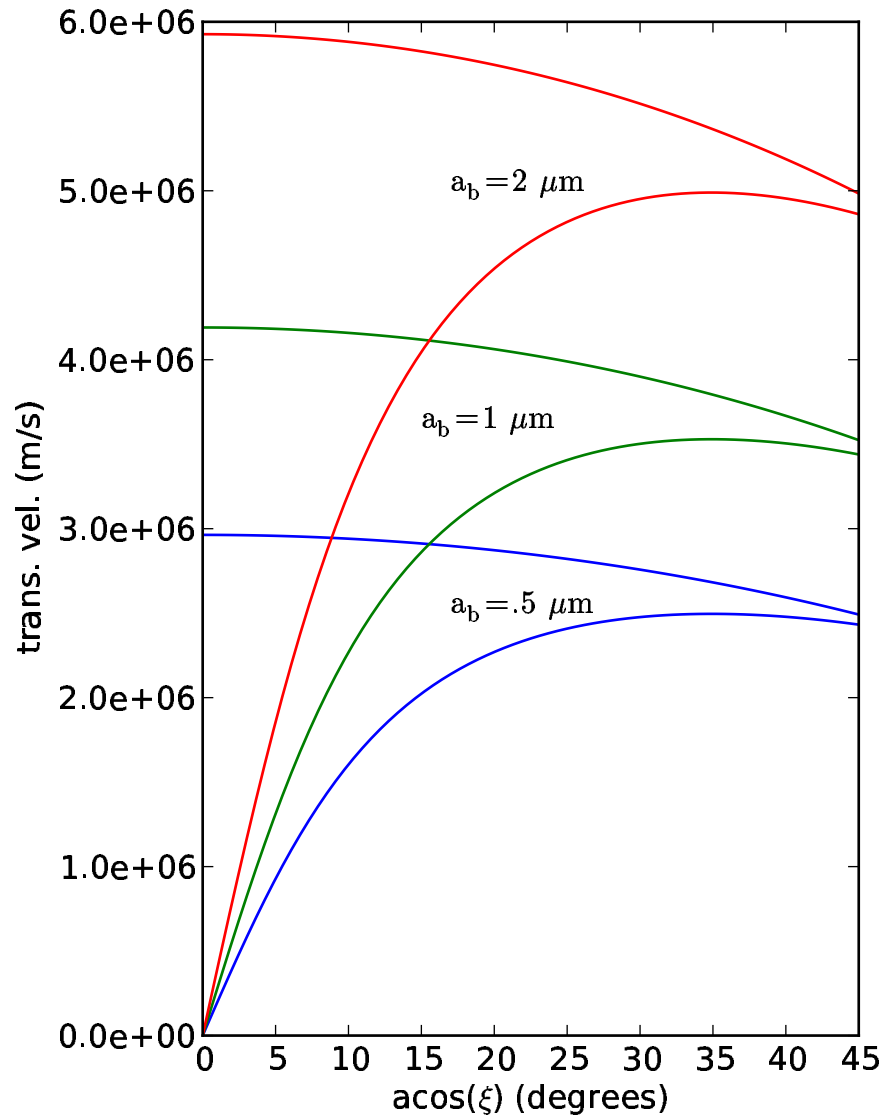
Figure 4.3: Effect of emitter height on the trajectories. Each calculated curve is paired with the corresponding upper bound (equation 3.1). The base radius in each case is one fifth the height. The applied field is 50 MV/m.
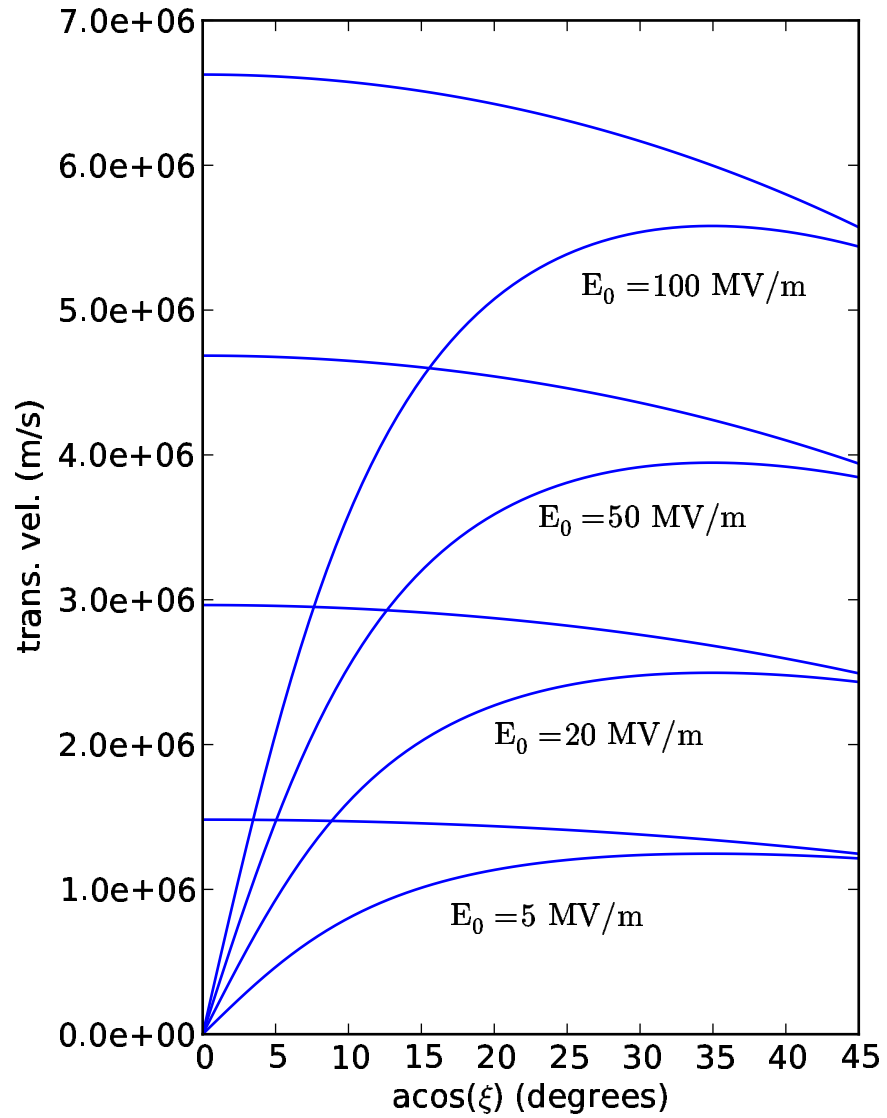
Figure 4.4: Effect of the magnitude of the applied field on the trajectories. Each calculated curve is paired with the corresponding upper bound (equation 3.1). For each case, the emitter height is 1.25 μm and the base radius is .25 μm

4.2 Sample emitter parameters

In the following sections, we examine how the properties of the emission distribution interact with the properties of the v_r–ξ distribution to determine the characteristics of the resulting transverse velocity distribution. The discussion is first narrowed to two sets of emitter parameters, each chosen to be paired with a certain peak cavity field. Here, the rationale behind the choice of examples is explained.

A combination of requirements must be taken into account in order to to define an appropriate emitter. A key limitation for field emission is the available field strength. For RF guns this is on the order of 100 MV/m at 2.85 GHz; for lower frequency structures, the limit is lower. Spindt cathodes are therefore ruled out because they require higher fields [15]. We instead focus on an emitter loosely resembling a diamond pyramid FEA as they operate at lower field, and their characteristics have been discussed specifically in the context this application [55]. The geometry we use is based on the diamond pyramid structures as described in [40]. These emitters consist of a pyramidal base with a narrow protrusion extending from the top. With only two parameters to adjust, the prolate spheroidal boss will be an extremely rough approximation of the true geometry.

The diamond pyramid we use as a reference has a height of .75 μm comprised of a .5 μm base and a .25 μm tip. The width of the base is .94 μm. The radius of curvature of the tip is reported to be 20 nm [21]. We choose the height and base radius of the boss so that its height and tip curvature match that of the diamond pyramid. As a result, the shape near the base is the least-well-modeled feature

of the real device. We justify this choice with the argument that, because of the distance between the tip and the base, the details of the geometry of the base would be expected to have the least effect on the fields near the tip. Applying this compromise, the base radius of a prolate spheroidal boss with height .75 μm and tip curvature of 20 nm is .12 μm (equation 2.13). The resulting field enhancement factor at the apex is 24.

The mechanism for field emission from diamond is theoretically more complex than for metals (see chapter 5 of [19]). In many instances, however, the basic Fowler-Nordheim equation is found to describe the current-voltage dependence for other materials with accuracy (see, for example, section 5.3 of [19]). Evidence that this is true for the diamond pyramids we are discussing, at least over a range of applied voltage, can be found reference [21], where a Fowler-Nordheim plot for these devices is shown. Using this simplification requires a value to be chosen for the work function parameter. We emphasize that there is no direct connection between the material properties of this diamond surface and the work function as it appears in the Fowler-Nordheim equation for metals. To get a rough estimate for this parameter, we note that the Vanderbilt group reports a single tip current of 15 μA at an applied field of 30 MV/m. Using the geometry of the boss we have established, the tip current can be found by numerical integration as described in appendix A, and by varying the work function it is found that a value of 1.15 eV results in a current of 18 μA. Because of the gross differences between the shape of the prolate spheroidal boss and the diamond pyramids, this value is more than likely not a close match to the true value, but it will serve as an adequate basis for the following discussion.

The emitter just described, which we will call emitter a, is designed to turn on at the lowest possible field. RF guns, particularly those that operate at higher frequencies, are capable of producing fields in excess of 100 MV/m. Because of the steep slope of the Fowler-Nordheim relationship, the first emitter would suffer damage well before that level is reached. Therefore, as a second example, we consider the hypothetical case of an emitter with material properties similar to the previous one, but with the field enhancement factor reduced by increasing the radius of curvature of the tip in order to facilitate its use at a higher applied field. Choosing a targed field of 80 MV/m, an emitter with height .75 μm, base radius .3 μm, and a work function of 1.15 eV will produce 33 μA. The radius of curvature of the tip for this geometry is 120 nm, and the field enhancement factor at the apex is 7.4. This emitter will be referred to as emitter b.

The parameters for the two emitters are compiled in table 4.1.

4.3 Emission distribution and v_r–ξ distribution for the sample emitters

As mentioned above, the transverse velocity distribution is the convolution of the current distribution and the v_r–ξ distribution. These distributions are plotted in matching pairs for selected magnitudes of the applied field in figures 4.5 and 4.6 for emitter a and emitter b respectively. As a consequence of the nearly vertical current-voltage relationship for field emission, for a given FEA, measurable emission only begins to occur as the applied field closely approaches the RF peak field. As
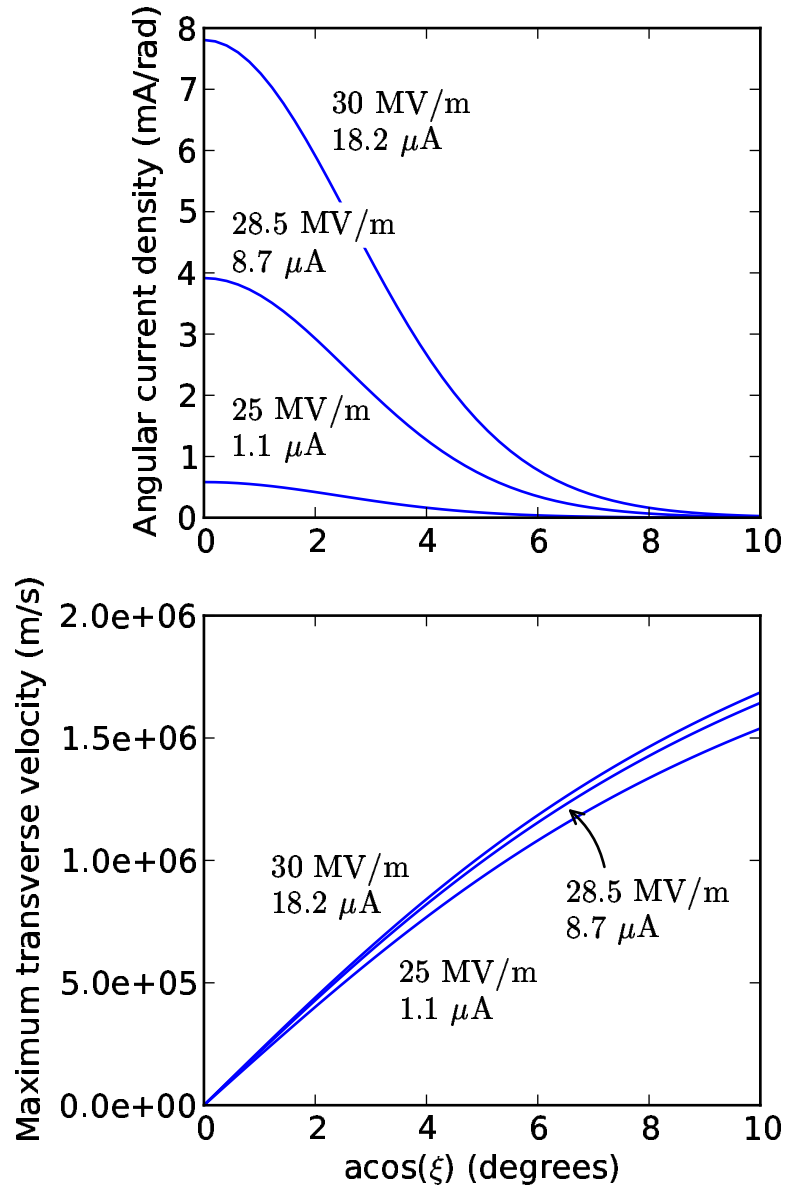
Figure 4.5: Current density distribution (top) and v_r–ξ distribution for emitter a plotted for three values of the applied field chosen to illustrate cases where the integrated current is low, intermediate, and high.
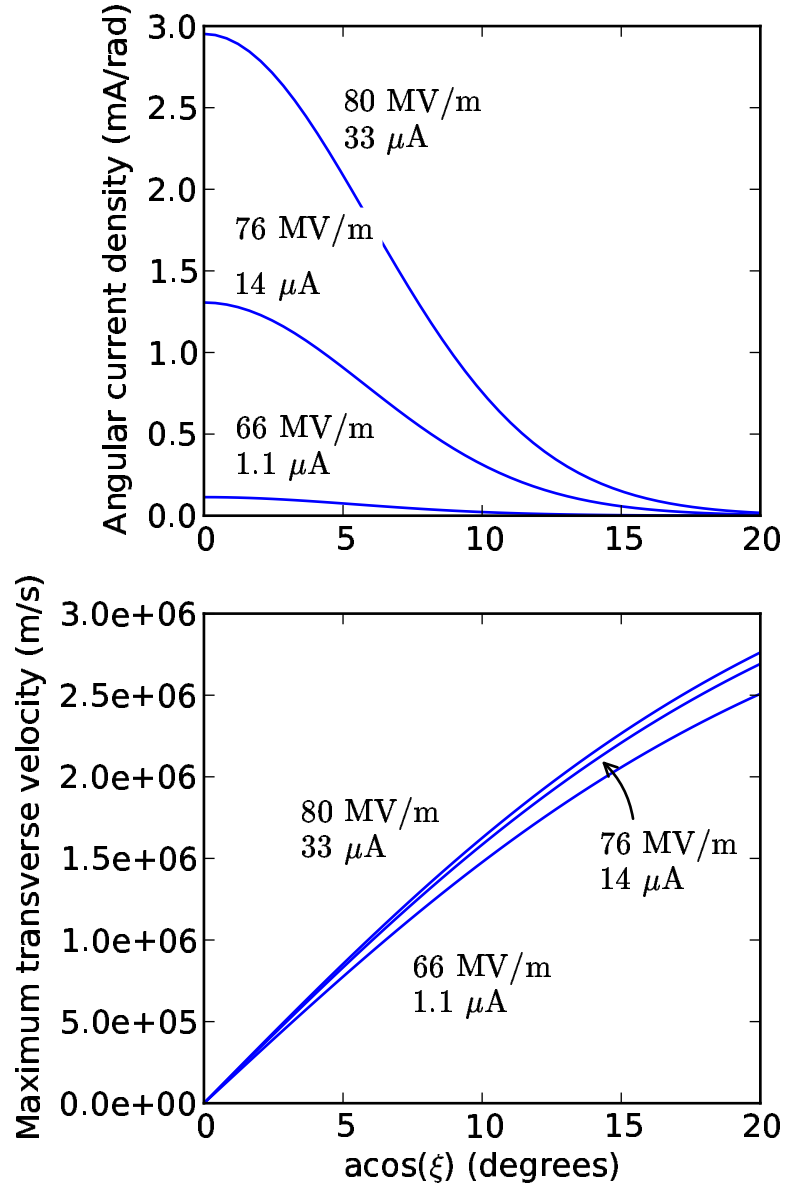
Figure 4.6: Current density distribution (top) and v_r–ξ distribution for emitter b plotted for three values of the applied field chosen to illustrate cases where the integrated current is low, intermediate, and high.

		emitter a	emitter b
Physical parameters			
Height	a_b	.75 μm	.75 μm
Base radius	b_b	.122 μm	.3 μm
Tip radius	c_r	20 nm	120 nm
Peak field enhancement	$\beta(0°)$	24	7.4
Effective work function	ϕ	1.15 eV	1.15 eV
"Operational" parameters			
Operating field	E_0	30 MV/m	80 MV/m
Peak current density	$J(0°)$	8.3×10^{10}A/m^2	5.2×10^9A/m^2
Total current	I	18 μA	33 μA

Table 4.1: Parameters for the sample emitters.

a result, two electrons launched at different RF phase but from the same point on the tip have nearly identical trajectories. A second observation is that, whereas the magnitude of the emission distribution changes significantly with applied field, the change in the width of the distribution is relatively modest. Taken together, these two observations suggest that the emittance will not change much during the pulse — a supposition which will later be confirmed.

Another useful piece of information can be ascertained from these figures. By considering a given pair of curves, it is possible to estimate the width of the resulting transverse velocity distribution. As an example, in figure 4.5, for the highest field case, the bulk of the current distribution falls within about 4° of the apex. Referencing this angle to the corresponding v_r–ξ distribution, the final transverse velocity for an electron emitted at 4° is roughly 8×10^5 m/s. We would therefore

expect the rms value of the transverse velocity distribution to be on this order.

4.4   Characterization of the transverse velocity distribution

Distributions for the transverse velocity as well as its Cartesian component v_x were calculated as described in appendix A.6. The results are plotted at different applied fields for emitter a in figure 4.7. Each curve is paired with a Maxwell-Boltzmann distribution with equivalent rms velocity. This data was also plotted for emitter b and other parameter sets; the qualitative characteristics of the distributions were found to be similar in all cases. The most striking feature is the close resemblance between the calculated distributions and the Maxwell-Boltzmann distributions. There is no obvious reason for this correspondence, although it seems to hold fairly generally for the prolate spheroidal boss model. Interestingly, though, experimental measurements on a DFEA cathode have found the same correspondence [22]. Still, there is no clear reason to expect this to be a universal characteristic of FEAs.

For the cases presented in the figure, we can compare the calculated value for $\tilde{v}_x$ to the theoretical upper bound given by equation 3.2. In the 25 MV/m case, the theoretical upper bound is U.B.$[\,\tilde{v}_x\,] = 1.8 \times 10^6$ m/s, 3.8 times the calculated value of 4.8×10^5 m/s. For the 30 MV/m case, the upper bound is U.B.$[\,\tilde{v}_x\,] = 2.0 \times 10^6$ m/s, 3.5 times the calculated value of 5.7×10^5 m/s.
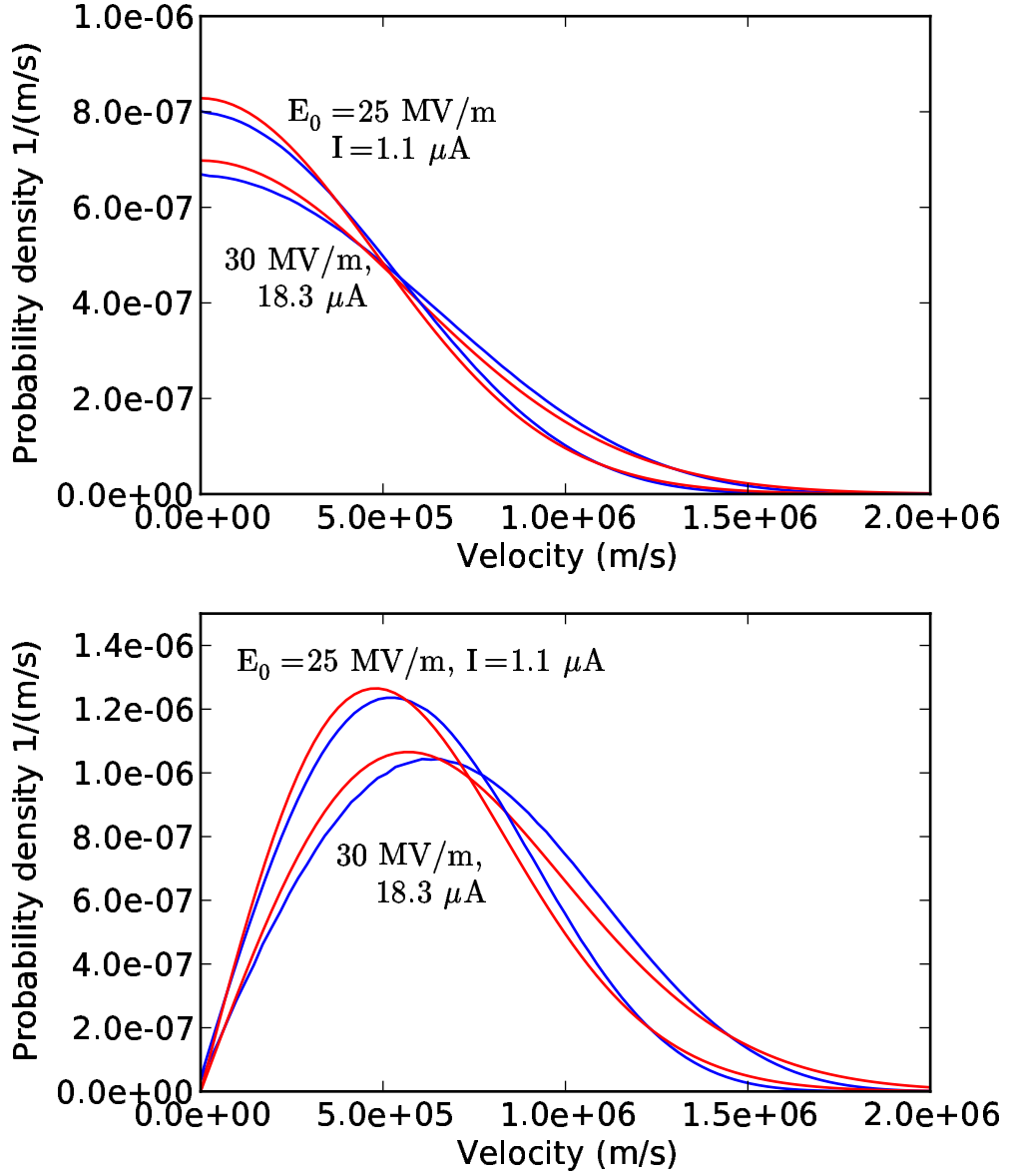
Figure 4.7: (top) Distribution of the x component of the velocity (blue) and one-dimensional Maxwell-Boltzmann distribution with equivalent $\tilde{v}_x$ (red) for emitter a at two operating points. At 25 MV/m, the emitter is just beginning turn on. Here, $\tilde{v}_x = 4.8 \times 10^5$ m/s, corresponding to kT = 1.3 eV. At 30 MV/m, a value chosen to represent the peak field that might be used with this emitter, $\tilde{v}_x = 5.7 \times 10^5$ m/s, corresponding to kT = 1.8 eV. (bottom) Distribution of $\tilde{v}_r$, the magnitude of the two dimensional transverse velocity vector (blue), and for the rms equivalent two-dimensional Maxwell-Boltzmann distribution (red). For the two dimensional case, the rms velocities are $\sqrt{2}$ times greater than the one-dimsional case, $\tilde{v}_r = 6.8 \times 10^5$ m/s at 25 MV/m and $\tilde{v}_r = 8.0 \times 10^5$ m/s at 30 MV/m. The equivalent temperature is the same.

65

4.5 Evolution of the velocity distribution during the RF cycle

Figure 4.8 illustrates how the beam properties evolve during the pulse for each sample emitter. As the current rises as the peak field is reached, the emittance increases as well. As had been inferred from earlier results in the chapter, the magnitude of the change in the emittance is not very large. The average emittance of the bunch is weighted towards the higher values because this is where the current is highest. Because the emittance is a function of field, an intrinsic emittance for a given FEA can not be precisely defined. The variation is small enough (on the order of 10% in these examples) as to be negligible in practice.
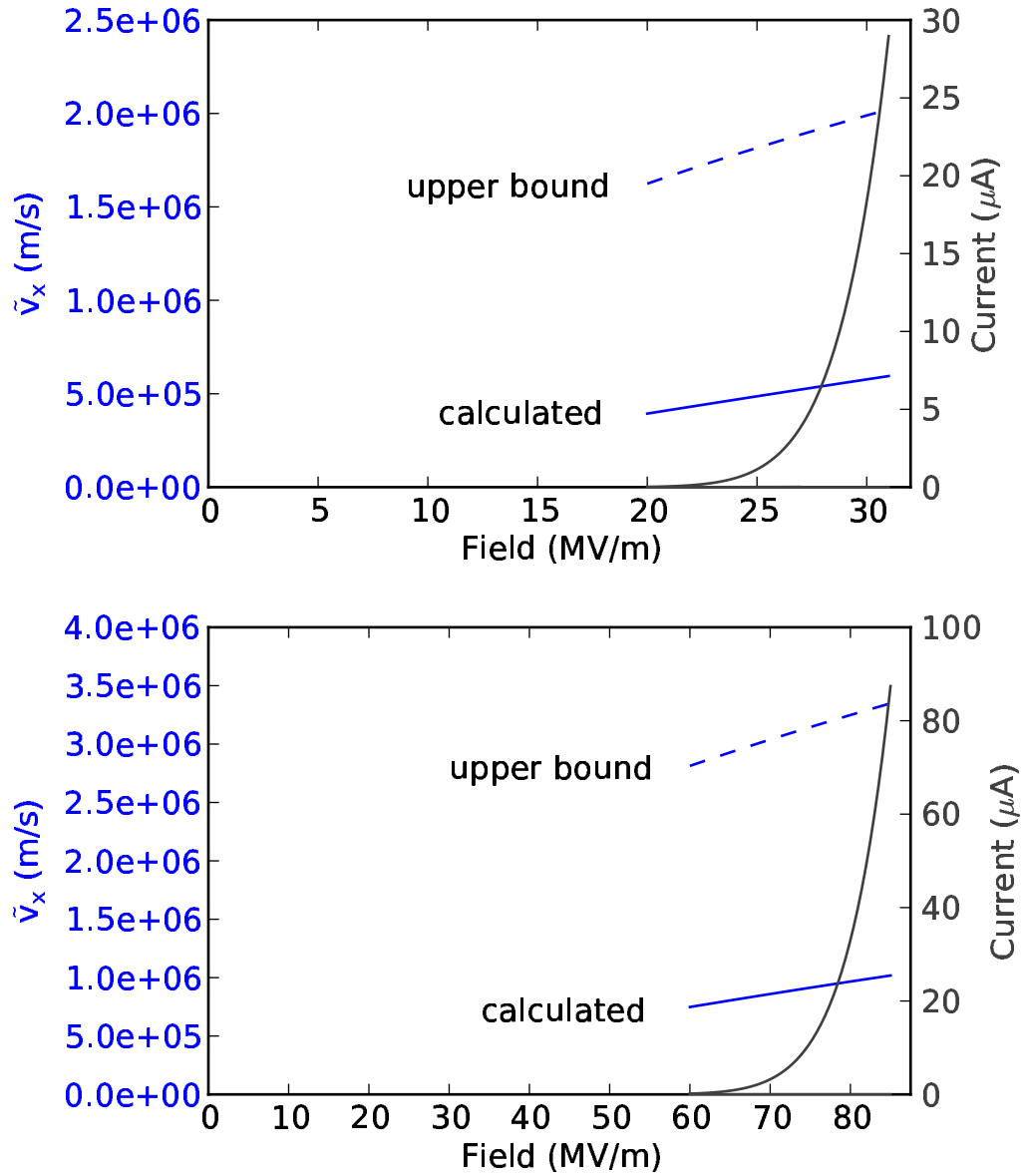
Figure 4.8: Variation of $\tilde{v}_x$ during the pulse for emitter a (top) and emitter b. Emittance depends linearly on $\tilde{v}_x$. The right-hand axis gives the integrated single-tip current.

Chapter 5

Temporal emission distribution and beam transport in the cathode
cell

Until now, we have focused on properties of the transverse distribution. In
this chapter, longitudinal dynamics will be considered. As with a thermionic cath-
ode gun, for an ungated field emitter, the cavity field determines both the timing
of emission and the resulting electron trajectories. Because the current-field rela-
tionship is more complex for field emission than for thermionic emission, we will see
that the cavity design will determine certain specifications which must be met by
the FEA. In other words, the cathode and cavity must be designed as a single unit.
Furthermore, because field emission rises so sharply, there are constraints on the
range of peak cavity field that can be used for a given cathode-gun combination.

For thermionic cathode guns, electrons emitted late in the RF cycle do not
reach the exit and are accelerated back into the cathode. This back bombardment
limits the duration of the RF pulse due to runaway heating of the cathode, and it
is an unwanted source of beam loading. For FEA cathodes, the risk of damaging
the emitters would be the main concern. It will be seen, though, that field emission
can be constrained to occur over a short enough range of RF phase that, with the
proper choice of cavity length, back bombardment will not occur.

Although, with an RF extraction field, emission occurs over a shorter time

period for field emission than for thermionic emission, the field-emitted pulse is still long in the sense that the bunch will exit the cathode cell with a large longitudinal energy spread. The best approach to manage this would depend on the requirements of the application. Several possibilities, both simple and more sophisticated, are mentioned at the end of the chapter.

5.1   Temporal distribution of emission

As a foundation for studying the longitudinal beam dynamics, the relationship between field-emitted current and RF phase must be known. The exact relationship depends on the details of the emitter, but a simplified analysis leads to reasonable expectations for the pulse duration. It is based on the behavior of the Fowler-Nordheim equation, which was plotted in figure 1.4. Because of the steep rise of the emission current with field, the emission is strongly peaked near the crest of the field. The range of phase over which the bulk of current is emitted is related to the ratio of the peak field to the threshold field by the sinusoidal time dependence of the cavity field as illustrated in figure 5.1. We must choose a value for the peak field for the analysis. For this purpose we will use the field where the current density predicted by the Fowler-Nordheim equation is 5×10^{11} A/cm^2, which represents a very strongly driven cathode (see chapter two of [13]). The cathode will emit over a larger region of phase the more strongly it is driven, but because of the steepness of the current-voltage relationship, the dependence is not strong. Another caveat is that, for sharp tips, the current-voltage relationship rises more even more

69
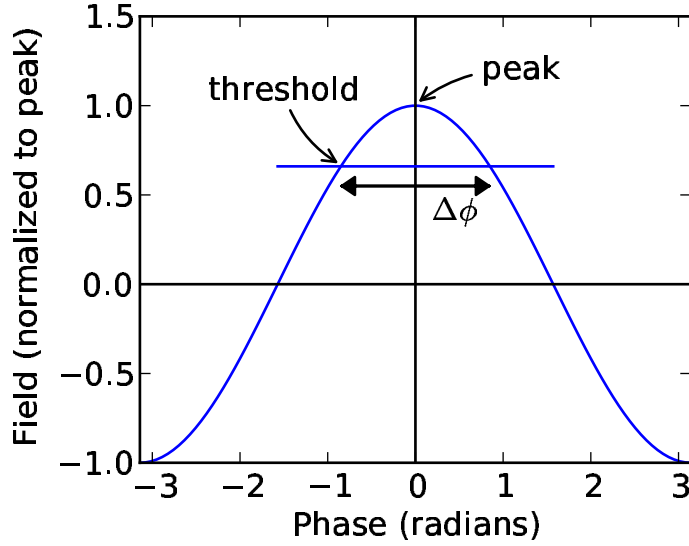
Figure 5.1: Field emission occurs once the field exceeds a given threshold. For a sinusoidal field, the range of phase over which emission occurs is the inverse cosine of the ratio of the threshold field to the peak field, as illustrated in this figure.

steeply than the one dimensional Fowler-Nordheim equation predicts because area over which emission occurs increases with increasing field (see section 3.3.1 of [12]). If the statistical distribution of emitter properties within the array is taken into account (some tips turn on before others because of slight their slight variations), the emission will be still more peaked [56]. This characterization based on the one dimensional theory can therefore only be used as a point of reference.

We use, as examples, the two values of work function plotted in the figure1.4. For the case of 2.5 eV work function, a current density of 5×10^{11} A/cm^2 is reached at a field of 3 GV/m (as a reminder, this refers to the field taking into account the field enhancement due to the sharp tip). The onset of significant emission occurs at roughly 2.5 GV/m. The bulk of the current is therefore emitted in the range of phase between $\pm \arccos (2.5/3.0) \approx \pm 30°$ of the crest. For the emitter with $\phi = 4.5$ eV,

5×10^{11} A/cm^2 is reached at a field of 7.5 GV/m, whereas emission begins to rise steeply at about 6.26 GV/m. The resulting range of phase is roughly the same. Becuase the general shape of the Fowler-Nordheim relationship is not very sensitive to the work function, it is not surprising that this calculation leads to the same results for a wide range of work functions. In the following analysis, it will thus be assumed the the pulse occupies the range of phase $\pm 30°$ of the crest.

As was demonstrated by Fontana and Shaw [57], the shape of the current pulse due to the RF field is approximately Gaussian. For the range of voltage where field emission current density is significant, the change in current with voltage in the approximate one dimensional Fowler-Nordheim equation (equation 1.7) is dominated by the exponential term, in other words

$$J\left(F\right) \approx C_1 \exp\left(-C_2 \frac{\phi^{\frac{3}{2}}}{F}\right)$$

where $C_2 = 6.5 \times 10^9$ and C_1 is not needed in what follows. To avoid ambiguity, we use F for the field at the surface of the cathode (taking into account field enhancement), whereas we will use E to denote the "macroscopic" field of the cavity. If the RF field at the cathode is given by $F = F_0 \cos\left(\omega_{\mathrm{RF}}t\right)$, this relationship becomes

$$J\left(F\right) \approx C_1 \exp\left(-\frac{C_2 \phi^{\frac{3}{2}}}{F_0} \sec\left(\omega_{\mathrm{RF}}t\right)\right).$$

Most emission occurs near the crest of the field, near $t = 0$. In this neighborhood, the Taylor series expansion for the secant function is $\sec x \approx 1 + .5x^2$, so

$$J\left(F\right) \approx C_1' \exp\left(-\frac{C_2 \phi^{\frac{3}{2}}}{F_0} \frac{\left(\omega_{\mathrm{RF}}t\right)^2}{2}\right),$$

in other words, the pulse is Gaussian with

$$\frac{1}{2\sigma^2} = \frac{C_2 \phi^{\frac{3}{2}}}{F_0} \frac{\omega_{\mathrm{RF}}^2}{2} \qquad \text{or} \qquad \frac{2\sigma}{\tau_{\mathrm{RF}}} = \frac{F_0^{\frac{1}{2}}}{\pi C_2^{\frac{1}{2}} \phi^{\frac{3}{4}}}$$

This quantity varies over a fairly limited range for realistic values of F_0 and ϕ. For the lower work function we have considered, $\phi = 2.5$ eV, substantial emission occurred in the neighborhood of $F = 2.75$ GV/m, so the range within $\pm\sigma$ covers about 10% of the RF period. For the higher work function emitter, where $\phi = 4.5$ eV, substantial emission occurred in the neighborhood of 7 GV/m, indicating $\pm\sigma$ covers roughly 11% of the RF period. In other words, the range between $\pm\sigma$ extends over about $\pm 36°$ of phase, a result, in the context of the approximations we have made, that does not vary much with work function or field strength. Other factors we have not considered, such as the aforementioned change of emission area with field for very sharp tips, could be expected to modify this result somewhat.

The pulse width as we have defined has turned out to to correspond to approximately 2σ in the Gaussian approximation. For a Gaussian curve, about 95% of the distribution falls within $\pm 2\sigma$, so the pulse width we have defined encompasses roughly that percentage of the total emission. Qualitatively speaking, if the cathode is driven harder, the pulse will be more sharply peaked, and it will also cover a greater phase range, whereas if the peak field is closer to the threshold, the pulse will be less peaked and also shorter relative to the RF period.
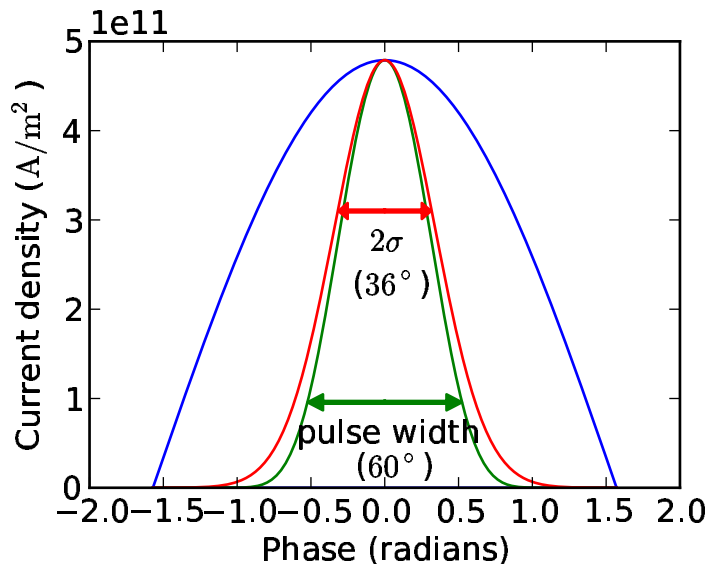
Figure 5.2: Pulse shape of electrons emitted from a field emission cathode in an RF field. The blue curve represents the RF field. The green curve is the current density as calculated using the approximate, one dimensional Fowler-Nordheim theory, where the green arrow shows the pulse width as defined above in the text. The red curve is the Gaussian approximation, where the red arrow shows the range covering one standard deviation to each side of the center.

5.2   Longitudinal dynamics in the cathode cell

In this section, we use the information about the timing of emission found in the previous section to study the longitudinal dynamics of the resulting bunch in the cathode cell of an RF gun.

As was discussed in the first chapter, most RF gun cavities are variations on a generic cylindrical pillbox excited at the TM_{010} mode. This mode has a longitudinal electric field component on the axis which is constant along the length of the axis and has a sinusoidal dependence on time,

$$E_z(t) = E_0 \cos(\omega_{RF} t).$$

It is this field that accelerates the electrons. The H_ϕ field component influences the off-axis electrons, but to a lesser degree than E_z. Here we consider only the dynamics associated with the primary accelerating field. Another caveat is that this field is only uniform along the axis for an ideal pillbox. Practical considerations (for instance, the necessity for a beam exit port) mean that this cavity geometry is never truly realized. Nevertheless, the results should give a fairly good representation of the expected behavior for a simple single-cell RF gun.

For an electron emitted at phase ϕ_L relative to the crest, the momentum after time t is

$$p(t) = \int_{t(\phi_L)}^{t_{\max}} e E_0 \cos(\omega_{\text{RF}} t')\, dt' = \frac{e E_0}{\omega_{\text{RF}}} \left[\sin(\omega_{\text{RF}} t) - \sin(\phi_L) \right] \qquad (5.1)$$

From the relativistic relationship $p = \text{mc}\beta\gamma$, we have

$$\beta = \frac{v}{\text{c}} = p \sqrt{\frac{1}{p^2 + \text{m}^2 \text{c}^2}}.$$

The trajectories can be found by integrating this equation with respect to time using the momentum given in equation 5.1. A closed form solution for this integral is only possible for this integral when $\phi_L = 0$. In other cases, approximations must be used [58]. Therefore, we turn to numerical solutions.

5.3   Longitudinal dynamics: numerical solutions

Figures 5.3, 5.4, and 5.5 show the on-axis longitudinal dynamics for electrons emitted from a field emission cathode for three different RF cavity configurations. In each case, the position of electrons emitted at various initial phases is plotted versus

phase. Paired with each of these is a corresponding plot of electron energy versus phase. The examples are chosen to illustrate gun design considerations specific to field emission cathodes. From the figures, several important pieces of information about the beam can be determined as a function of cavity length (or, more generally, distance from cathode to exit port in the case of a reentrant cavity), such as pulse length, beam energy and energy spread, and electron back-bombardment. It is assumed a separate FEA is chosen to match the conditions of each scenario in line with the discussion earlier in the chapter. In other words, an FEA that is appropriate when the peak field is 30 MV/m would not be suitable when the peak field is 80 MV/m.

Figure 5.3 shows that, for a 2.85 GHz cavity operated at a peak field of 80 MV/m, a quarter-cell cavity (where the length is one eighth of the free space wavelength) would allow virtually all of the emitted current to exit the cavity, implying little or no back-bombardment. Electrons at the head of the pulse would exit the cavity with the highest energy, 1 MeV, while electrons at the tail would exit with the lowest energy, 310 keV. Electrons emitted at the crest, where the current is highest, reach 800 keV. At the exit of the gun, the pulse length is essentially unchanged from when it is emitted, $2\sigma \approx 30°$ of phase ≈ 30 ps, though after exiting the gun, the pulse would expand rapidly due to the large energy spread.

Figure 5.4 is a solution for a 1 GHz cavity operated at a peak field of 30 MV/m (Lower frequency cavities are limited to lower peak fields [29]). The result is qualitatively similar to the previous example. Again, little or no back-bombardment would occur. We again consider a quarter-cell cavity. At the exit, electrons at the head
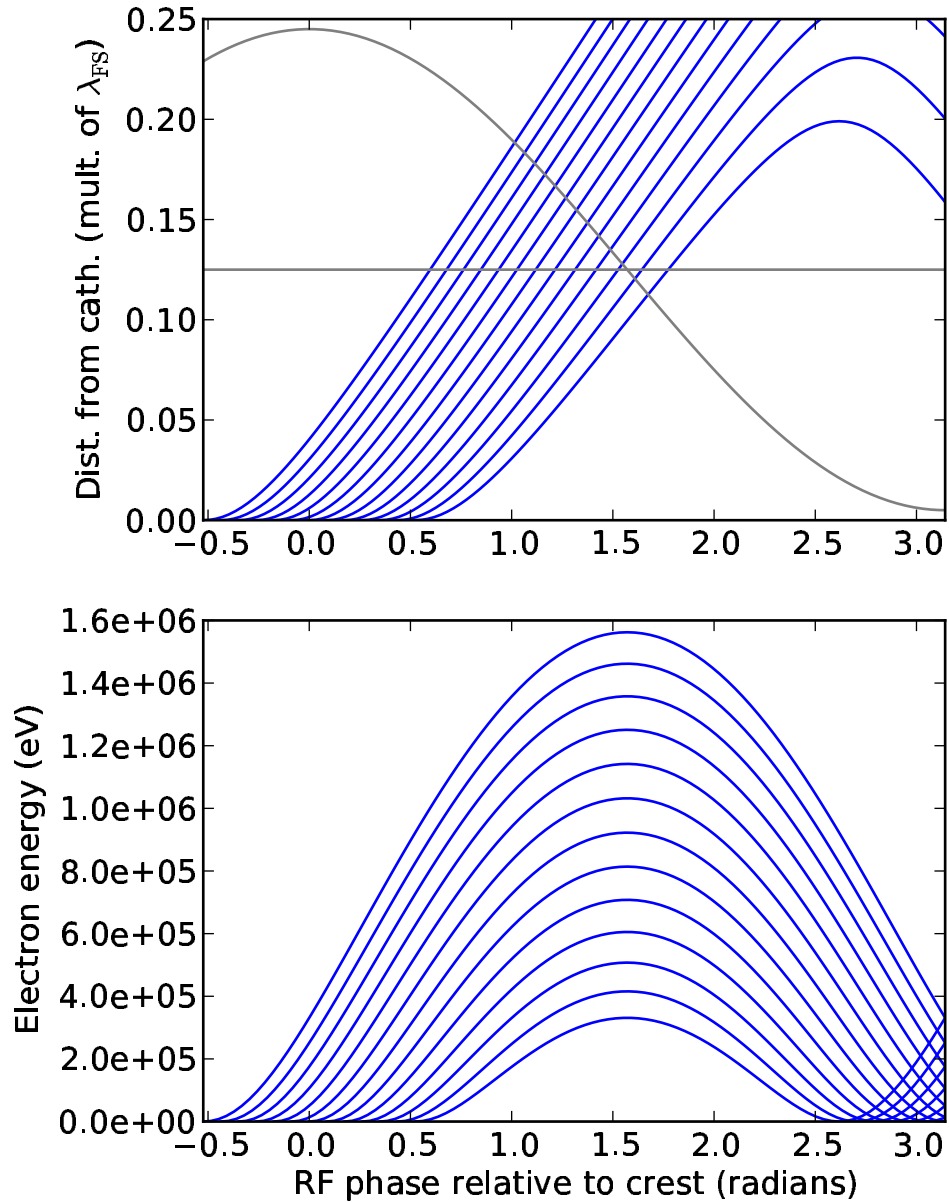
Figure 5.3: Trajectories (top) and kinetic energy (bottom) for electrons accelerated in an 2.85 GHz pillbox cavity with a peak field of 80 MV/m. The phase of the RF field is superimposed on the top figure. The central trajectory corresponds to an electron launched at the crest of the field. The separation between the trajectories is 5°. The leftmost trajectory is launched 30° ahead of the crest, while the rightmost is emitted 30° behind. Over 90% of the total current is emitted within this time. Distance is normalized to the free space wavelength, which, at 2.85 GHz, is λ_{FS} = .11 m. The period is 350 ps.

of the bunch would reach 1.1 MeV, at the tail, 350 keV, and electrons emitted on crest, 950 keV. The pulse length at the exit of the gun is $2\sigma \approx 30°$ of phase ≈ 80 ps.

Figure 5.5 shows a solution at the same frequency as the first example (2.85 GHz), but with a lower peak field (30 MV/m). The effect of the interrelationship between emission timing and particle dynamics inherent to field emission cathodes used in combination with RF acceleration is seen. For a photoinjector, the pulse would be triggered further in advance of the crest, so that the electrons would experience greater total acceleration. For a thermionic cathode RF gun, some current is guaranteed to be emitted at the optimal phase. For the FEA, emission occurs only near the crest, which in this case leads to a low energy beam and the occurrence of back-bombardment.

5.4 Discussion

Some of the principles that must be considered when designing a cavity for an FEA cathode-based electron gun have been highlighted. An important observation is that the gun can be designed so that back bombardment, which limits the average beam power produced by a thermionic cathode RF gun, is eliminated. It therefore may be possible to run this type of gun at high average power. To be cautious, it should be noted that the emission profile has short tails, so it is not out of the question that some small amount of current would return to the cathode. It is not yet known how cathodes such as DFEAs would be affected by electron bombardment.

We conclude this chapter by mentioning a few possible configurations for an
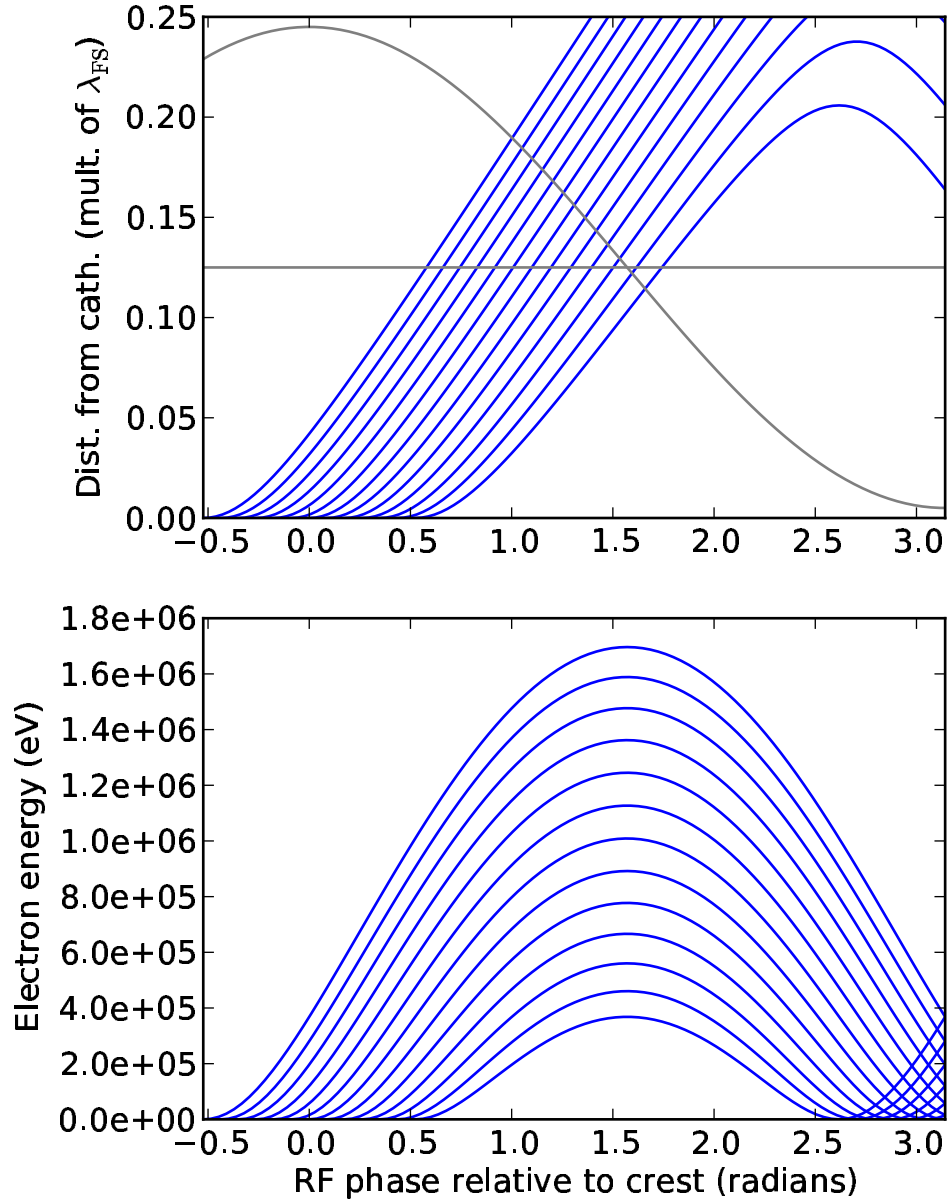
Figure 5.4: Same as figure 5.3, except the cavity frequency is lower and the peak field is lower. Trajectories (top) and kinetic energy (bottom) for electrons accelerated in an 1 GHz pillbox cavity with a peak field of 30 MV/m. The phase of the RF field is superimposed on the top figure. The central trajectory corresponds to an electron launched at the crest of the field. The separation between the trajectories is 5°. The leftmost trajectory is launched 30° ahead of the crest, while the rightmost is emitted 30° behind. Over 90% of the total current is emitted within this time. Distance is normalized to the free space wavelength, which, at 1 GHz, is $\lambda_{FS} = .3$ m. The period is 1 ns.
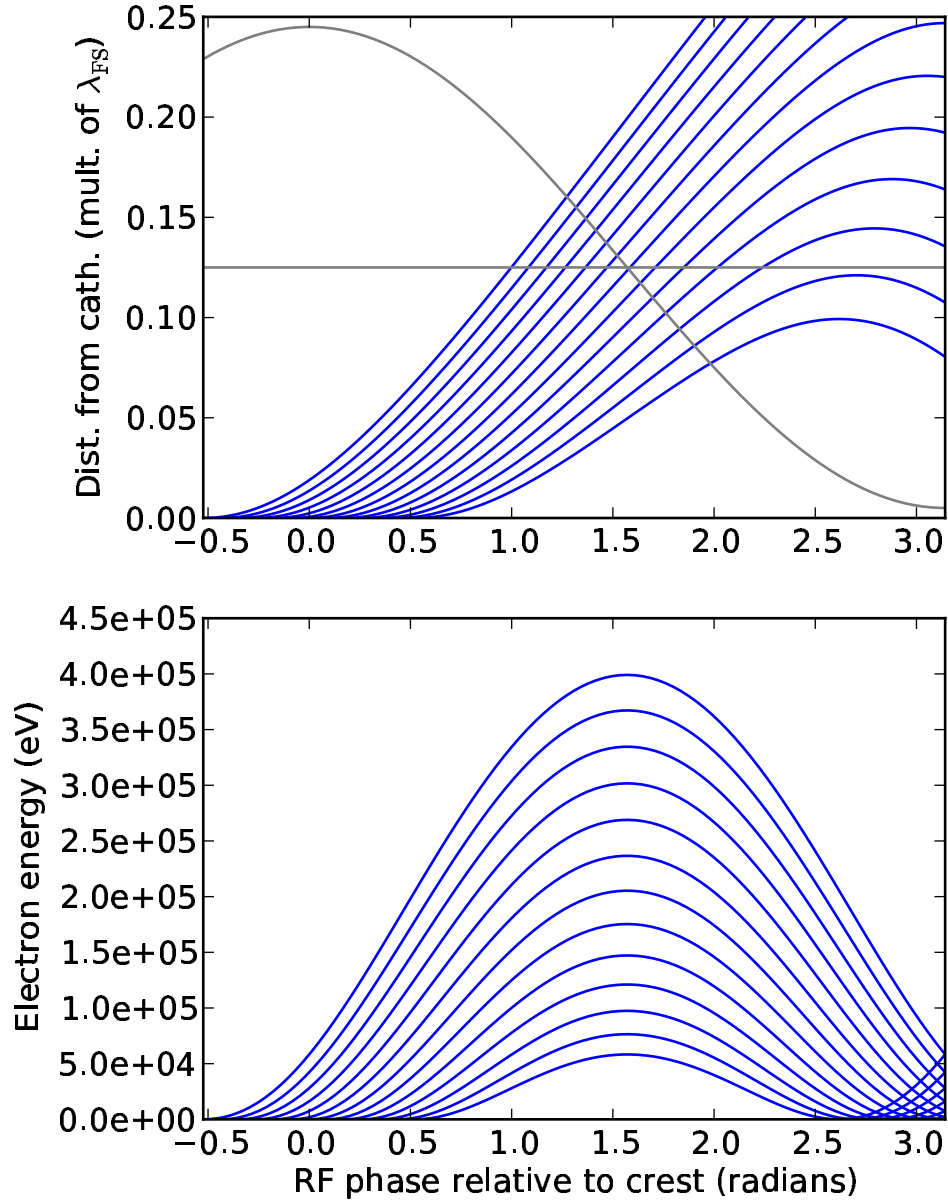
Figure 5.5: Same as figure 5.3, but the peak field is lower — the cavity frequency is again 2.85 GHz. Trajectories (top) and kinetic energy (bottom) for electrons accelerated in an 2.85 GHz pillbox cavity with a peak field of 30 MV/m. The phase of the RF field is superimposed on the top figure. The central trajectory corresponds to an electron launched at the crest of the field. The separation between the trajectories is 5°. The leftmost trajectory is launched 30° ahead of the crest, while the rightmost is emitted 30° behind. Over 90% of the total current is emitted within this time. Distance is normalized to the free space wavelength, which, at 2.85 GHz, is $\lambda_{FS} = .11$ m. The period is 350 ps.

FEA-based injector.

1. The simplest approach would be to operate an FEA cathode-based gun like a thermionic cathode RF gun. In this case, the gun is followed by an α-magnet [59] to compress the bunch. Within the α-magnet, the transverse location of each electron is correlated with its energy, so it is possible to scrape off part of the beam to reduce its energy spread. Potential advantages over the thermionic cathode would be the elimination of back-bombardment, and the fact that field emission cathodes may be capable of producing higher current density.

2. A second possibility would be the dual-frequency design suggested by Lewellen and Noonan [32] (described in section 1.6). Here, the bunch length is determined by the period of the third harmonic, so it is one third the length it would be if it were gated by the cavity fundamental. Because the bunch is shorter compared to the period of the fundamental, there is less variation in the trajectories from the head of the bunch to the tail, so the energy spread is lower. Also, by advancing the phase of the third harmonic relative to the fundamental, the beam dynamics can be optimized. There do, however, remain challenges to designing and coupling power into a dual-frequency cavity.

3. A third option might be to operate the gun at the third harmonic of the injector, and to follow it with a cavity that kicks every third bunch into the injector. The bunch length would be shorter relative to the RF period of the rest of the accelerator and thus more manageable, but the energy spread would

be large compared to the dual-frequency approach, and it is unlikely that all the current could be captured. Still, this configuration could potentially yield some advantages over the first approach.

Chapter 6

Observations, future work, and conclusions

We begin this chapter by making several observations that combine results from earlier chapters.

6.1   General conclusions about the intrinsic emittance of FEAs

Over the course of chapters 3 and 4, emittance measurements based on two sets of experiments for two different cathode types were evaluated, as were calculations based on two different emitter models. The upper bound we have described provides a context within which to make comparisons between these diverse examples. For instance, the intrinsic emittance of the DFEA pyramids was quite close to the upper bound for that geometry, whereas the intrinsic emittance of $TaSi_2$ rods was several times below their corresponding upper bound. This type of comparison will be useful in identifying possible connections between emitter properties and intrinsic emittance, which could then be verified with simulations. As a specific example, compared against a $TaSi_2$ rod, the tip of a DFEA pyramid is sharper relative to the dimensions of its base. Based on this observation, Jensen's model [15] could be used to study the effect of varying the tip curvature while holding other parameters constant, a type of analysis for which that model is ideally suited. This could in turn be used to optimize the design of the emitters.

6.2 Comparisons between cathode types

In chapter 5, it was seen that field emission is distributed over a narrower range of phase than thermionic emission but a much broader range of phase than photoemission. In this sense, an FEA gun is more aptly compared to a thermionic cathode gun than a photocathode gun. It was seen that the intrinsic emittance of an FEA cathode scales roughly with the square root of field; considering a tip height of 1 μm, an applied field of 30 MV/m, and taking the emittance to be one third of the upper bound (consistent with the majority of the examples we have seen), the effective temperature of the distribution is on the order of 5 eV. At 80 MV/m, the effective temperature would be about 2.6 times higher. Although these temperature values are much higher in absolute terms than the thermionic case (where kT $\approx$ 100 meV), emittance scales as the square root of effective temperature, so for the 30 MV/m case the emittance is expected to be $\sqrt{5/.1} \approx 7$ times higher (or 11.5 times higher in the 80 MV/m case). In practical terms, this analysis overstates the difference in performance between the two cathodes, because the extremely low intrinsic emittance exhibited by a thermionic cathode can not be perfectly preserved during acceleration.

So far, we have assumed the two emitters are the same size, but Diamond pyramid FEAs have demonstrated current densities 10 times higher than the typical thermionic cathode (over 100 A/cm^2 [23] versus a typical value of 10 A/cm^2 [4], p. 12). By reducing the radius of the FEA cathode by a factor of $\sqrt{10} \approx 3$, its emittance is reduced by the same factor, and the same current as the original size thermionic

cathode is generated. With the caveat that high current density DFEAs are still a young technology, the gap between the emittance performance of the two cathodes is quite narrow.

In cases where low emittance is not a limiting factor, the much higher potential current densities for FEAs is a significant advantage. Also, thermionic cathode guns have average power limitations due to back bombardment, whereas this does not appear to be an issue for field emission cathodes. On the other hand, the reliability of thermionic cathodes is beyond question, but DFEA cathodes have never been tested in an RF gun. In principle, the diamond surface is chemically inert, a property that tests in DC and pulsed guns has confirmed. As experience with photocathodes has amply demonstrated, however, an RF gun can be a troublesome environment in which to maintain the properties of an emitting surface.

As a final point of reference, we compare FEA cathodes with photocathodes. Because these emission mechanisms are not as closely related as thermal emission and field emission, the comparisons to be made are of a more general nature. In practical applications, the effective temperature of an electron bunch generated by photoemission is in the range of 100 meV–1 eV. The beam brightness that can be achieved with a photocathode gun is much greater than for field emission sources. In fact, the limitation on brightness for a photoemission source is not the emission process itself, the limit is instead reached when space charge forces cause unmanageable expansion of the beam. A significant drawback for photocathode guns is complexity. They require sophisticated drive lasers, and many photocathode types must be fabricated in-situ.

6.3   Summary of key results

- An upper bound on the intrinsic emittance of an FEA cathode was found. In many cases, this will allow an immediate determination of whether or not an FEA could be used for a specified application.

- The upper bound was compared against emittance data reported in a variety of experimental and numerical studies. A wide variety of emitter types were represented in the examples. The upper bound was found to fall 1–4 times above the exact values in these cases, but there is not sufficient evidence to consider that range a general rule.

- As Liu and Lau [35] determined from their study of the two-dimensional wedge, our results for general two or three-dimensional structures indicate the emittance scales by the square root of the emitter height and applied field. (Liu and Lau added the caveat that the effect of these parameters on beam brightness is indeterminate.)

- In chapter 4, it was found that the transverse velocity distribution for electrons emitted from a prolate spheroidal boss-shaped emitter is very similar to the Maxwell-Boltzmann distribution. This relationship was also observed in experiments conducted by Jarvis et al. [22].

- Field emission extracted with an RF field has a characteristic temporal distribution. By calculating on-axis electron trajectories based those initial conditions, it was shown that it is possible to design an FEA cathode gun where

back bombardment does not occur. Therefore, high average power operation appears to be feasible.

6.4 Future work

The investigations carried out to date lead naturally to several areas for future study:

- The prolate spheroidal boss model employed in chapter 5 is relatively limited. Jensen's model for FEA emittance calculation should be used to gain an improved understanding of the connection between emitter characteristics and the upper bound on emittance.

- Because of the extremely high electron density that exists near the emitter tips, the effect of Coulomb collisions on the distribution can become significant. This is known as the Boersch effect [60, 4]. The impact of the Boersch effect should be investigated.

- Space charge can affect both the emitted current density and the electron trajectories. In the first case, a dense space-charge cloud can reduce the field at the emitter surface, limiting the emission. Jensen [61] and others have studied this effect. The effect on the electron trajectories can be separated into two regimes: near the tip, where the charge density is large, but the external field is very strong, and downstream from the cathode, where both are lower in magnitude. Jensen has estimated that the impact of the first of

these is minimal [15]. The second effect, the expansion of the beamlets due to space charge during transit in the cavity, must still be investigated.

6.5   Conclusions

The application of field emission cathodes to RF guns, interest in which has been recently been spurred by advances in FEA fabrication techniques, is a technology primed for rapid development. Already, novel gun concepts exploiting the unique characteristics of field emitters have been proposed [32]. For this type of gun to be built, one prerequisite is that a full understanding of the temporal and transverse properties of emission from FEA cathodes must be attained. Knowing these characteristics will give an initial indication of the applications for which FEA guns would be well suited. Furthermore, they will determine certain aspects of the cavity design. In this dissertation, we have summarized the known characteristics of FEA emission that are relevant to this application, and we have begun to fill in some of the gaps in that knowledge. As a result, a clearer picture of how an ungated FEA cathode based gun might be implemented has begun to take shape.

Appendix A

Numerical solutions using Python

In chapter 6, numerical solutions for the equations of motion for an electron accelerated in the electrostatic field created in the presence of a prolate spheroidal boss were presented. In this appendix, we describe how these calculations were carried out. The programs or scripts used were implemented in Python, making use of the Numpy and Scipy packages.

A.1   Solving the equations of motion

The Python `odeint` function was used to integrate the equations of motion [62]. `odeint` is a wrapper for the LSODA ODE integrator [63], which is part of the `odepack` package developed at Lawrence Livermore National Laboratory [64]. In all cases, the default arguments were used.

The equations of motion are

$$
\frac{d^2r}{dt^2} = \frac{F_r}{m} = -\frac{eE_r}{m}
$$
$$
\frac{d^2z}{dt^2} = \frac{F_z}{m} = -\frac{eE_z}{m}
$$

The ODE solver requires the equations to be rewritten in standard form, as a system

of first-order equations:

$$\frac{dr}{dt} = v_r$$

$$\frac{dv_r}{dt} = -\frac{eE_r}{m}$$

$$\frac{dz}{dt} = v_z$$

$$\frac{dv_z}{dt} = -\frac{eE_z}{m}.$$

The electric field is found by taking the gradient of the potential,

$$\mathbf{E}\left(r, z\right) = -\nabla\,\Phi\left(r, z\right) = \left(-\frac{\partial}{\partial r}\Phi\right)\,\hat{\mathbf{r}} + \left(-\frac{\partial}{\partial z}\Phi\right)\,\hat{\mathbf{z}}.$$

The potential, equation 2.11, is

$$\Phi\left(r, z\right) = \mathrm{E}_0 z \left[1 - \frac{\dfrac{\eta\,\mathrm{acoth}\left(\eta\right) - 1}{\eta}}{\dfrac{\eta_{\mathrm{b}}\,\mathrm{acoth}\left(\eta_{\mathrm{b}}\right) - 1}{\eta_{\mathrm{b}}}}\right]$$

$$\eta\left(r, z\right) = \frac{\sqrt{r^2 + \left(z - \mathrm{f_b}\right)^2} + \sqrt{r^2 + \left(z + \mathrm{f_b}\right)^2}}{2\mathrm{f_b}}$$

giving

$$\mathrm{E_r}\left(r, z\right) = -\mathrm{E}_0 \frac{z}{\dfrac{\eta_{\mathrm{b}}\,\mathrm{acoth}\left(\eta_{\mathrm{b}}\right) - 1}{\eta_{\mathrm{b}}}} \left(\frac{1}{\eta^2\left(\eta^2 - 1\right)}\right) \times$$

$$\frac{1}{2\mathrm{f_b}} \left(\frac{r}{\sqrt{r^2 + \left(z - \mathrm{f_b}\right)^2}} + \frac{r}{\sqrt{r^2 + \left(z + \mathrm{f_b}\right)^2}}\right)$$

and

$$\mathrm{E_z}\left(r, z\right) = -\mathrm{E}_0 \left\{1 - \frac{\dfrac{\eta\,\mathrm{acoth}\left(\eta\right) - 1}{\eta}}{\dfrac{\eta_{\mathrm{b}}\,\mathrm{acoth}\left(\eta_{\mathrm{b}}\right) - 1}{\eta_{\mathrm{b}}}} + \right.$$

$$\left. \frac{z}{\dfrac{\eta_{\mathrm{b}}\,\mathrm{acoth}\left(\eta_{\mathrm{b}}\right) - 1}{\eta_{\mathrm{b}}}} \left(\frac{1}{\eta^2\left(\eta^2 - 1\right)}\right) \frac{1}{2\mathrm{f_b}} \left(\frac{z - \mathrm{f_b}}{\sqrt{r^2 + \left(z - \mathrm{f_b}\right)^2}} + \frac{z + \mathrm{f_b}}{\sqrt{r^2 + \left(z + \mathrm{f_b}\right)^2}}\right)\right\}$$

The function `odeint` takes as input a user-supplied function that, given the state variables of the system at the current time step, returns a vector comprised of the time derivatives of the variables. For this problem, the state variables are r, v_r, z, and v_z. `odeint` uses the time derivatives to calculate the state of the system at the next time step. This process is repeated until the specified final time is reached. We have implemented the required function as follows.

```
def calcTimeDerivs(state_vec, time, E0, f, nb0):

    r, vr, z, vz = state_vec

    Q1 = lambda x: x*.5*math.log((x+1.0)/(x-1.0))-1.0
    dt = lambda x,y: math.sqrt(x**2+(y-f)**2)
    db = lambda x,y: math.sqrt(x**2+(y+f)**2)

    nb = (.5/f)*(dt(r,z)+db(r,z))

    Eta = z/(Q1(nb0)/nb0)
    Etb  = 1.0/((nb**2)*((nb**2)-1.0))

    Ert = r/dt(r,z) + r/db(r,z)
    dvrdt = (q/m)*E0*Eta*Etb*(.5/f)*Ert

    Ezt1 = (Q1(nb)/nb)/(Q1(nb0)/nb0)
    Ezt2 = (z-f)/dt(r,z) + (z+f)/db(r,z)
    dvzdt = (q/m)*E0*(1.0-Ezt1+Eta*Etb*(.5/f)*Ezt2)

    time_derivs = [vr, dvrdt, vz, dvzdt]
    return time_derivs
```

A.2 Determining the final transverse velocity of a trajectory

After the ODE solver is used to calculate a trajectory, the final transverse velocity for the trajectory is simply the v_r component at the final time step. Because the electric field is discontinuous at the surface of the boss, it is necessary to nudge

the electron's initial position off of the boss by a small factor. The ODE solver

takes the initial values for the state variables, together with an array of time values,

and returns the values of the state variables at each time. For the calculations

we carried out, the trajectories were calculated to a time of 1.5 ps, for which v_r

converged within an acceptable margin in all cases. The implementation of this

process is shown below.

```
def VrMax(xi, nb, f, E0, t_max):

    nudge = 1.000000001
    t_npts = 100

    t_array = numpy.linspace(0,t_max,num=t_npts)

    r0 = nudge*f*math.sqrt((1.0-xi**2)*(nb**2 - 1.0))
    z0 = nudge*f*nb*xi
    state_vec_init = [r0, 0, z0, 0]

    ode_soln =  spi.odeint(calcTimeDerivs, state_vec_init, t_array,
                    args=(E0, f, nb))
    return ode_soln[-1,1]
```

A.3   Area integrals in prolate spheroidal coordinates

Certain calculations, such as velocity distributions and the total current emit-

ted from a tip, require integration over a section of the spheroidal surface. The

differential area element for this case ($\eta =$ constant) is given by

$$dA = h_\xi h_\phi d\xi d\phi$$

where ϕ is the azimuth angle. The scale factors h_ξ and h_ϕ are (see p. 1284 of reference [65])

$$h_\xi = f_b \sqrt{\frac{\eta_b^2 - \xi^2}{1 - \xi^2}} \qquad \text{and} \qquad h_\phi = f_b \sqrt{(\eta_b^2 - 1)(1 - \xi^2)}$$

where the roles of η and ξ are reversed from the reference. Therefore,

$$dA = f_b^2 \sqrt{(\eta_b^2 - 1)(\eta_b^2 - \xi^2)}.$$

When integrating a generic surface density $\delta(\eta, \phi)$ over a surface S, we thus have

$$\iint_S \delta(\eta, \phi) \; f_b^2 \sqrt{(\eta_b^2 - 1)(\eta_b^2 - \xi^2)} \; d\xi d\phi.$$

In Python, we have implemented the expression $f_b^2 \sqrt{(\eta_b^2 - 1)(\eta_b^2 - \xi^2)}$ as

```python
def dA_factor(xi, f, nb):
    return 2*math.pi*(f**2)*math.sqrt((nb**2-xi**2)*(nb**2-1.0))
```

When the problem has azimuthal symmetry, the azimuthal integral can be carried out immediately, leaving

$$\iint_S \delta(\eta, \phi) \, dA = 2\pi \int_{\xi_1}^{\xi_2} \delta(\eta) \; f_b^2 \sqrt{(\eta_b^2 - 1)(\eta_b^2 - \xi^2)} \; d\xi.$$

A.4   Current density and integrated current

The current density at a given point, given by the Fowler-Nordheim equation, is determined by the applied field and the field enhancement factor. The field enhancement factor for the prolate spheroidal boss was given in equation 2.12. It is implemented as

```python
def beta(nb, xi):
    return (1.0/(nb*.5*math.log((nb+1.0)/(nb-1.0))-1.0))*xi/ \
        math.sqrt((nb**2-1.0)*(nb**2-xi**2))
```

We use the simplified version of the Fowler-Nordheim equation as defined in equation 1.7, implemented as

```
fnc1 = 1.4e-6
fnc2 = 9.8
fnc3 = 6.5e9

def current_density(xi, E0, nb, wrkfn):
    F = E0*beta(nb, xi)
    t1 = fnc1*(F**2)/wrkfn
    t2 = math.exp(fnc2/math.sqrt(wrkfn))
    t3 = math.exp(-1.0*fnc3*(wrkfn**1.5)/F)
    return t1*t2*t3
```

The total current emitted by a tip is found by integrating the current density determined by the Fowler-Nordheim equation across the surface of the emitter. Because the emission falls off rapidly as the distance from the apex increases, it is possible to integrate over a restricted range of θ. Choosing `theta_max` to be $20°$ was sufficient for all of the cases we encountered. This integral is implemented as

```
didxi_fn = lambda xi: current_density(xi, E0, nb, wrkfn) * \
            diffA_factor(xi, f, nb) * 2.0 * math.pi
total_current = spi.quad(didxi_fn, math.cos(theta_max), 1)
```

A.5   Calculating RMS velocity

When the mean of a distribution is zero, its rms value is equal to its standard deviation. The standard deviation of a function $f(\mathbf{x})$ defined on a two-dimensional surface S, weighted by an unnormalized density function $\delta(\mathbf{x})$, is defined by

$$\sigma^2 = \iint_S f(\mathbf{x}) \frac{\delta(\mathbf{x})}{\iint_S \delta(\mathbf{x}) dA} dA = \frac{\iint_S f(\mathbf{x})\delta(\mathbf{x}) dA}{\iint_S \delta(\mathbf{x}) dA}, \qquad (A.1)$$

93

where the integral in the denominator normalizes the density function so that it takes the form of a probability density function.

To calculate the rms velocity of the electrons emitted from an emitter, $f(\mathbf{x})$ becomes the distribution of final transverse velocities $v_r(\xi, \phi)$, and the weighting function $\delta(\mathbf{x})$ becomes the current distribution $j(\xi, \phi)$. The scale factors for the surface integral were given in the previous section. Equation A.1 becomes

$$\tilde{v_r}^2 = \frac{\iint_S v_r(\xi, \phi)^2 \, j(\xi, \phi) \, f_b^2 \sqrt{(\eta_b^2 - 1)(\eta_b^2 - \xi^2)} \, d\xi d\phi}{\iint_S j(\xi, \phi) \, f_b^2 \sqrt{(\eta_b^2 - 1)(\eta_b^2 - \xi^2)} \, d\xi d\phi}.$$

The transverse velocity distribution has azimuthal symmetry, so the ϕ integral simply contributes a factor of 2π to both the numerator and denominator, such that

$$\tilde{v_r}^2 = \frac{\int_{\xi_1}^{\xi_2} v_r(\xi, \phi)^2 \, j(\xi, \phi) \, f_b^2 \sqrt{(\eta_b^2 - 1)(\eta_b^2 - \xi^2)} \, d\xi}{\int_{\xi_1}^{\xi_2} j(\xi, \phi) \, f_b^2 \sqrt{(\eta_b^2 - 1)(\eta_b^2 - \xi^2)} \, d\xi},$$

where $\xi_1 = \cos 0° = 1$ and $\xi_2 = \cos \theta_{\text{max}}$. As described in section A.4, θ_{max} is chosen to speed the processing time, with $\theta_{\text{max}} = 20°$ used for our computations.

To find $\tilde{v}_x$, $\tilde{v_r}^2$ is replaced by $(\tilde{v}_r \cos \phi)^2$. This is the only ϕ dependence in the numerator, so the integral in ϕ becomes $\int_0^{2\pi} (\cos^2 \phi) d\phi = \pi$. The integral in ϕ in the denominator again contributes a factor of 2π. In other words, $\tilde{v}_x^2 = .5 \, \tilde{v}_r^2$.

The calculation of $\tilde{v}_r$ is implemented in Python as

```
Evr2_integrand = lambda xi: (VrMax(xi,nb,f,E0,t_max))**2 * 2 * math.pi \
    current_density(xi, E0, nb, wrkfn) * diffA_factor(xi, f, nb)
Evr2 = spi.quad(Evr2_integrand, math.cos(theta_max), 1)

didxi_fn = lambda xi: current_density(xi, E0, nb, wrkfn) * \
    diffA_factor(xi, f, nb) * 2.0 * math.pi
total_current = spi.quad(didxi_fn, math.cos(theta_max), 1)

v_rms = math.sqrt(Evr2[0]/total_current[0])
```

A.6 Calculating the velocity distributions

The velocity distributions were calculated in a straight forward if inelegant manner. The range covered by the velocities was broken into bins, and the emitting surface was broken into small area elements. For each element, a contribution proportional to the total current emitted from that element was made to the bin corresponding to the final transverse velocity for trajectories originating in the center of the element. For the v_x distribution, the area elements were sectioned in both ξ and ϕ, and v_x for each element was set to $v_r \cos \phi$. The implementation of this is shown below. The implementation for v_r, not shown, is essentially the same, except, because v_r is independent of ϕ, the area simply consisted of strips corresponding to small ranges of ξ, therefore the inner loop is not required.

```
nbins = 100

vr_xi_array = numpy.cos(numpy.linspace(math.cos(xi_max), 0, 400))
vr_list = [VrMax(xi, nb, f, E0, t_max) for xi in vr_xi_array]
vr_array = numpy.array(vr_list)
max_vrmax = numpy.amax(vr_array)

phi_max = math.pi/2.0
N_phi = 2000
d_phi = phi_max / N_phi

N_xi = 2000
xi_array = numpy.cos(numpy.linspace(math.acos(xi_max), 0, N_xi))

v_values = numpy.linspace(0, max_vrmax, num=nbins)
v_bin_locs = numpy.linspace(0, max_vrmax+max_vrmax/
              (nbins-1), num=nbins+1)
vx_weights = numpy.zeros(nbins)
for i in range(N_xi - 1):
    xi_mid = (xi_array[i] + xi_array[i+1]) / 2.0
    d_xi = xi_array[i+1] - xi_array[i]
    vr = numpy.interp([xi_mid], vr_xi_array, vr_array)[0]
```

```
    cd = current_density(xi_mid, E0, nb, wrkfn)
    dA = diffA_factor(xi_mid, f, nb) * d_xi * d_phi
    for j in xrange(N_phi):
        phi_mid = (float(j)+.5) * d_phi
        vx = vr * math.cos(phi_mid)
        weight = cd * dA
        vx_bin = numpy.digitize([vx], v_bin_locs)[0] - 1
vx_weights[vx_bin] += 2 * weight
```

Bibliography

[1] G.A. Westenskow and J.M.J Madey, "Microwave electron gun," Laser and Particle Beams 2, 223 (1984).

[2] R.L. Sheffield, "Photocathode RF Guns," in *Physics of Particle Accelerators* (AIP Conference Proc. 184), 1500 (1988)

[3] J.D. Jackson, *Classical Electrodynamics*, 3rd ed., (John Wiley & Sons, Inc., New York, 1999), ch. 8.

[4] M. Reiser, *Theory and Design of Charged Particle Beams* (John Wiley & Sons, New York, 1994).

[5] P.G. O'Shea, "Reversible and irreversible emittance growth," Phys. Rev. E 57, 1081 (1998).

[6] C.A. Brau, "What Brightness Means," in *The Physics of High Brightness Electron Beams*, J. Rosenzweig and L. Serafini, Eds., World Scientific, Singapore (2003), p. 20.

[7] M.J. Rhee, "Refined definition of the beam brightness," Phys. Fluids. B 4, 1674 (1992).

[8] D. Temple, "Recent progress in field emitter array development for high perfromance applications," Materials Science and Engineering: R: Reports 25, 185 (1999).

[9] E.L. Murphey and R.H. Good, "Thermionic emission, field emission, and the transition region," Phys. Rev. 102, 1464 (1956).

[10] C.A. Spindt, I. Brodie, L. Humphrey, and E.R. Westerberg, "Physical properties of thin-film field emission cathodes with molybdenum cones," J. Appl. Phys. 47, 5248 (1976).

[11] K.L. Jensen, *Electron Emission Physics* (Academic Press, San Diego, 2007).

[12] K.L. Jensen, "Theory of Field Emission," in *Vacuum Microelectronics*, W. Zhu, ed., (John Wiley & Sons, New York, 2001), ch. 3.

[13] G. Fursey, *Field Emission in Vacuum Microelectronics* (Kluwer Academic / Plenum Publishers, New York, 2005).

[14] P.H. Cutler, J.H. He, N.M. Miskovsky, T.E. Sullivan, and B. Weiss, "Theory of electron emission in high fields from atomically sharp emitters: validity of the Fowler-Nordheim equation," J. Vac. Sci. Tecnol. B 22, 387 (1993).

[15] K.L. Jensen, P.G. O'Shea, D.W. Feldman, and J.L. Shaw, "Emittance of a field emission electron source," J. Appl. Phys. 107, 014903 (2010).

[16] J. Shaw and J. Itoh, "Silicon field emitter arrays," in *Vacuum Microelectronics*, W. Zhu, ed., (John Wiley & Sons, New York, 2001), ch. 5.

[17] I. Brodie and P.R. Schwoebel, "Vacuum microelectronic devices," Proc. IEEE 82 (1994).

[18] "Spindt Field Emitter Arrays," in *Vacuum Microelectronics*, W. Zhe, ed., (John Wiley & Sons, New York, 2001), ch. 4.

[19] W. Zhu, ed., *Vacuum Microelectronics* (John Wiley & Sons, New York, 2001).

[20] W. Zhu, P.K. Baumann, C.A. Bower, "Novel Cold Cathode Materials," in *Vacuum Microelectronics*, W. Zhe, ed., (John Wiley & Sons, New York, 2001), ch. 6.

[21] W.P. Kang, J.L. Davidson, M. Howell, B. Bhuva, D.L. Kinser, and D.V. Kerns, "Micropatterned polycrystalline diamond field emitter vacuum diode arrays," J. Vac. Sci. Technol. B 14, 2068 (1996).

[22] J.D. Jarvis, H.L. Andrews, C.A. Brau, B.K. Choi, J. Davisdon, B. Ivanov, W.-P. Kang, C.L. Stewart, and Y.-M. Wong, "Pulsed uniformity conditioning and emittance measurements of diamond field-emitter arrays," J. Vac. Sci. Technol. B 27, 2264 (2009).

[23] Y.M. Wong, W.P. Kang, J.L. Davidson, B.K. Choi, N. Ghosh, M. Howell, J.D. Jarvis, H.L. Andrews, and C.A. Brau, "Diamond field emission arrays (DFEAs) for high-power free electron lasers," 22nd Intl. Vacuum Nanoelectronics Conf., 203 (2009).

[24] J.D. Jarvis, H.L. Andrews, C.A. Brau, B.K. Choi, J. Davisdon, W.-P Kang, and Y.-M. Wong, "Uniformity conditioning of diamond field emitter arrays," J. Vac. Sci. Technol. B 27, 2264 (2009).

[25] F.M. Charbonnier, J.P. Barbour, L.F. Garrett, and W.P. Dyke, "Basic and applied studies of field emission at microwave frequencies," Proc. IEEE 51, 991 (1963).

[26] D.R. Whaley, B.M. Gannon, C.R. Smity, C.M. Armstrong, and C.A. Spindt, "Application of field emitter arrays to microwave power amplifiers," IEEE Trans. Plasma Sci. 28, 727 (2000).

[27] K.L. Jensen, "Field emitter arrays for plasma and microwave source applications," Phys. Plasmas 6, 2241 (1999).

[28] R.B. Marcus, T.S. Ravi, T. Gmitter, K. Chin, D. Liu, W.J. Orvis, D.R. Ciarlo, C.E. Hunt, and J. Trujillo, "Formation of silicon tips with < 1 nm radius," Appl. Phys. Lett. 56, 236 (1990).

[29] W.D. Kilpatrick, "Criterion for vacuum sparking designed to include both rf and dc," Rev. Sci. Instrum. 28, 824 (1957).

[30] C. Travier, "Rf guns: bright injectors for FEL," Nucl. Instr. Methods A 304, 285 (1991).

[31] A. Gasper, C. Piel, T. Weis, A. Göhl, T. Habermann, and G. Müller, "An S-band test cavity for a field emission based RF-gun," in *Proc. of the 6th European Particle Accelerator Conf.*, Stockholm, 1998, 1471.

[32] J.W. Lewellen and J. Noonan, "Field-emission cathode gating for rf electron guns," Phys. Rev. ST Accel. Beams 8, 033502 (2005).

[33] R. Ganter *et al.*, "Low emittance gun project based on field emission," Proc. 2004 FEL Conf., Trieste, 2004, 602.

[34] A. Oppelt *et al.*, "Towards a low emittance x-ray FEL at PSI," Proc. FEL 2007, Novosibirsk, 2007, 224.

[35] Y. Liu and Y.Y. Lau, "An evaluation of the intrinsic emittance of a field emitter," J. Vac. Sci. Technol. B 14, 2126 (1996).

[36] K.L. Jensen, P. Mukhopadhyay, E.G. Zaidman, K. Nguyen, M.A. Kodis, L. Malsawma, C. Hor, "Electron emission from a single spindt-type field emitter: comparison of theory with experiment," Appl. Surf. Sci. 111, 204 (1997).

[37] K.L. Jensen, Y.Y. Lau, D.W. Feldman, and P.G. O'Shea, "Electron emission contributions to dark current and its relation to microscopic field enhancement and heating in accelerator structures," Phys. Rev. ST Accel. Beams 11, 081001 (2008).

[38] K.L. Jensen, "Space charge, emittance, trajectories and the modeling of field emitter arrays," to appear in J. Vac. Sci. Technol. B.

[39] D.A. Kirkpatrick, G.L. Bergeron, M.A. Czarnaski, R.C. Davidson, H.P. Freund, J.J. Hickman, A. Manofsky, K.T. Tsang, J.M. Schnur, M. Levinson, and B.M. Ditchek, "High brightness electron beam sources for FEL applications," Nucl. Instr. Methods A318, 349 (1992).

[40] J.D. Jarvis, H.L. Andrews, C.A. Brau, B.K. Choi, J. Davidson, W. Kang, S. Raina and Y.M. Wong, "Transverse emittance of diamond field-emitter arrays," Proceedings of the 2008 Free Electron Laser Conference, `https://accelconf.web.cern.ch/accelconf/FEL2008/papers/tupph014.pdf`.

[41] M.J. Rhee and K.A. Boulais, "Root-mean-square emittance of mulitple beam systems," Phys. Fluids. B 3, 1781 (1993).

[42] T.E. Everhart, "Simplified analysis of point-cathode electron sources," J. Appl. Phys. 38, 4944 (1967).

[43] W.P. Dyke, J.K. Trolan, W.W. Dolan, and G. Barnes, "The field emitter: fabrication, electron microscopy, and electric field calculations," J. Appl. Phys. 24, 570 (1953).

[44] K.L. Jensen and E.G. Zaidman, "Field emission from an elliptical boss: Exact and approximate forms for area factors and currents," J. Vac. Sci. Technol. B 12, 776 (1994).

[45] J. He, P.H. Cutler, N.M. Miskovsky, T.E. Feuchtwang, T.E. Sullivan, M. Chung, "Derivation of the image interaction for non-planar pointed emitter geometries: application to field emission IV characteristics," Surf. Sci. 246, 348 (1991).

[46] L.H. Pan, T.E. Sullivan, V.J. Peridier, P.H. Cutler, and N.M. Miskovsky, "Three-dimensional electrostatic potential, and potential energy barrier, near a tip-base junction," Appl. Phys. Letters 65, 2151 (1994).

[47] K.L. Jensen, E.G. Zaidman, M.A. Kodis, B. Goplen, and D.N. Smithe, "Analytical and seminumerical models for gated field emitter arrays. I. Theory," J Vac. Sci. Technol. B 14, 1942 (1996).

[48] D.A. Kirkpatrick, A. Mankofsky, and K.T. Tsang, "Analysis of field emission from three-dimensional structures," Appl. Phys. Lett. 60, 2065 (1992).

[49] E.W. Weisstein, "Ellipse," `mathworld.wolfram.com/Ellipse.html`

[50] W.R. Smythe, *Static and Dynamic Electricity, 3rd ed.* (Hemisphere Publishing Corporation, New York, 1989) sec. 5.28 p. 177.

[51] E.W. Weisstein, "Prolate Spheroidal Coordinates," `mathworld.wolfram.com/ProlateSpheroidalCoordinates.html`

[52] P.M. Morse and H. Feshbach, *Methods of Theoretical Physics, Part I* (McGraw-Hill Book Company, New York, 1953).

[53] H. Kosmahl, "Analytic evaluation of field emission enhancement factors for ellipsoidal cones and elliptic cross-section wedges," IEEE Trans. Electron Devices 38, 1534 (1991).

[54] R.D. Young, "Theoretical total-energy distribution of field-emitted electrons," Phys. Rev. 113, 110 (1959).

[55] J.D. Jarvis, H.L. Andrews, C.A. Brau, B.K. Choi, J. Davisdon, W. Kang, S. Raina, and Y.M. Wong, "Development of diamond field-emitter arrays for free-electron lasers," Proceedings of the 2008 Free Electron Laser Conference, `http://cern.ch/AccelConf/FEL2008/papers/thaau04.pdf`.

[56] K.L. Jensen and C.M. Marrese-Reading, "Emission statistics and the characterization of array current," J. Vac. Sci. Technol. B 21, 412 (2003).

[57] J.R. Fontana and H.J. Shaw, "Harmonic Generation at Microwave Frequencies Using Field-Emission Cathodes," Proc. IRE 46, 1424 (1958).

[58] K.J. Kim, "Rf and space-charge effects in laser-driven rf electron guns," Nucl. Instr. Methods A275, 201 (1989).

[59] H.A. Enge, "Achromatic magnetic mirror for ion beams," Rev. Sci. Instrum. 34, 385 (1963).

[60] J. Qiang, J. Corlett, S. Lidia, H.A. Padmore, W. Wan, A. Zholents, M. Zolotorev, and A. Adelmann, "Numerical study of Coulomb scattering effects on electron beam from a nano-tip," Proc. 2007 Particle Accelerator Conf., 1185 (2007).

[61] K.L. Jensen, "Space charge effects in field emission: Three dimensional theory," J. Appl. Phys. 107, 014905 (2009).

[62] `http://www.scipy.org/Cookbook/CoupledSpringMassSystem`

[63] docs.scipy.org/doc/scipy/reference/generated/scipy.integrate.quad.html.

[64] A.C. Hindmarsh, "Serial Fortran solvers for ODE initial value problems," https://computation.llnl.gov/casc/odepack/odepack_home.html.

[65] P.M. Morse and H. Feshbach, *Methods of Theoretical Physics, Part II* (McGraw-Hill Book Company, New York, 1953).